

Spring 1995

# Experimental and numerical studies on pattern formation in electrochemical deposition

Zhenqiu Liu

*University of New Hampshire, Durham*

Follow this and additional works at: <https://scholars.unh.edu/dissertation>

---

## Recommended Citation

Liu, Zhenqiu, "Experimental and numerical studies on pattern formation in electrochemical deposition" (1995). *Doctoral Dissertations*. 1845.

<https://scholars.unh.edu/dissertation/1845>

This Dissertation is brought to you for free and open access by the Student Scholarship at University of New Hampshire Scholars' Repository. It has been accepted for inclusion in Doctoral Dissertations by an authorized administrator of University of New Hampshire Scholars' Repository. For more information, please contact [nicole.hentz@unh.edu](mailto:nicole.hentz@unh.edu).

## INFORMATION TO USERS

This manuscript has been reproduced from the microfilm master. UMI films the text directly from the original or copy submitted. Thus, some thesis and dissertation copies are in typewriter face, while others may be from any type of computer printer.

**The quality of this reproduction is dependent upon the quality of the copy submitted.** Broken or indistinct print, colored or poor quality illustrations and photographs, print bleedthrough, substandard margins, and improper alignment can adversely affect reproduction.

In the unlikely event that the author did not send UMI a complete manuscript and there are missing pages, these will be noted. Also, if unauthorized copyright material had to be removed, a note will indicate the deletion.

Oversize materials (e.g., maps, drawings, charts) are reproduced by sectioning the original, beginning at the upper left-hand corner and continuing from left to right in equal sections with small overlaps. Each original is also photographed in one exposure and is included in reduced form at the back of the book.

Photographs included in the original manuscript have been reproduced xerographically in this copy. Higher quality 6" x 9" black and white photographic prints are available for any photographs or illustrations appearing in this copy for an additional charge. Contact UMI directly to order.

# UMI

A Bell & Howell Information Company  
300 North Zeeb Road, Ann Arbor, MI 48106-1346 USA  
313/761-4700 800/521-0600



**EXPERIMENTAL AND NUMERICAL STUDIES ON  
PATTERN FORMATION IN ELECTROCHEMICAL  
DEPOSITION**

BY

Zhenqiu Liu

B.S. in Chemical Engineering (1983)  
M.S. in Chemical Engineering (1986)  
South China University of Technology  
Guangzhou, China

DISSERTATION

Submitted to the University of New Hampshire  
in partial fulfillment of  
the requirements for the degree of

Doctor of Philosophy

in

Engineering

May 1995

**UMI Number: 9528767**

---

**UMI Microform 9528767**

**Copyright 1995, by UMI Company. All rights reserved.**

**This microform edition is protected against unauthorized  
copying under Title 17, United States Code.**

---

**UMI**

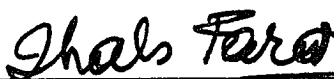
**300 North Zeeb Road  
Ann Arbor, MI 48103**

This dissertation has been examined and approved.



---

Dissertation director, Dr. Dale P. Barkey  
Associate Professor of Chemical Engineering



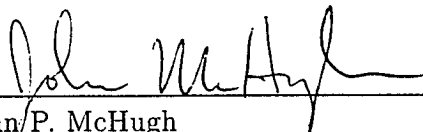
---

Dr. Ihab H. Farag  
Professor of Chemical Engineering



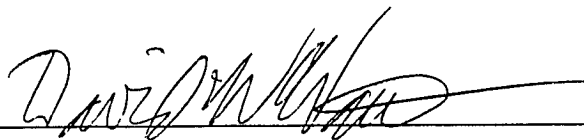
---

Dr. Palligarnai T. Vasudevan  
Associate Professor of Chemical Engineering



---

Dr. John P. McHugh  
Associate Professor of Mechanical Engineering



---

Dr. David W. Watt  
Associate Professor of Mechanical Engineering

January 20, 1995

Date

# Dedication

To Mom and Dad

# Acknowledgments

I would like to take this opportunity to express my gratitude to my advisor, Dr. Dale P. Barkey for his sincere assistance, consistent encouragement and excellent guidance throughout this project.

Special thanks to Dr. David W. Watt for his excellent guidances and assistance in setting up the interferometric facilities and in performing data analysis.

I would also like to thank Dr. Ihab H. Farag, Dr. Palligarnai T. Vasudevan, Dr. John P. McHugh and Dr. David W. Watt for serving on the dissertation committee and for their valuable advice and suggestions.

I am grateful to Dr. Vincent Fleury for attending my dissertation defence, for his valuable comments and discussion on this dissertation.

I would like to appreciate Mr. Jonathan E. Newell for his timely help during this project.

I would like to express my appreciation to Dr. Francesc Sagues for his valuable comments and discussion on this dissertation.

Finally, I express my deepest appreciation to my wife, Chiaoyun, my son, George, my parent, Zhenjie and Peixin, and my sisters, Buyun and Zihong for their love, emotional support and understanding.

This work was supported by the Natural Science Foundation, under Grant No. CTS-8915745 and No. CTS-9306837.



# Table of Contents

Dedication . . . . .	iii
Acknowledgments . . . . .	iv
Abstract . . . . .	xiv
<b>1 Introduction</b>	<b>1</b>
1.1 Purpose of Study . . . . .	1
1.2 Outstanding Issues . . . . .	2
1.2.1 Velocity and Morphology of Growth . . . . .	2
1.2.2 Role of Electrochemistry . . . . .	2
1.2.3 Role of Convection . . . . .	3
<b>2 Literature Review</b>	<b>4</b>
2.1 Definition of Morphology Selection . . . . .	4
2.2 Dendritic Growth in Solidification . . . . .	6
2.2.1 Theoretical Model . . . . .	6
2.2.2 Experimental Studies . . . . .	8
2.3 Pattern Formation in Hele-Shaw Cells . . . . .	9
2.3.1 Theoretical Model . . . . .	9
2.3.2 Experimental Studies . . . . .	10
2.4 Electrochemical Deposition . . . . .	11
2.4.1 Theory of Electrochemical Deposition . . . . .	12
2.4.2 Experimental and Theoretical Studies . . . . .	15
2.5 Theory of Velocity Selection . . . . .	18

<b>3</b>	<b>Experimental</b>	<b>20</b>
3.1	Electrochemical Deposition . . . . .	20
3.1.1	Experimental Setup Overview . . . . .	20
3.1.2	Apparatus and Materials . . . . .	21
3.1.3	Procedures . . . . .	26
3.2	Interferometry . . . . .	27
3.2.1	Digital Phase-Shifted Mach-Zehnder Interferometer . . . . .	27
3.2.2	Magnification . . . . .	29
3.2.3	Velocity of Aggregate Growth . . . . .	29
3.2.4	Accuracy of the Concentration Measurement . . . . .	29
<b>4</b>	<b>Results and Discussion</b>	<b>31</b>
4.1	Morphologies . . . . .	31
4.1.1	Copper Aggregates . . . . .	31
4.1.2	Zinc Aggregates . . . . .	35
4.2	Concentration Profiles . . . . .	39
4.2.1	Copper Deposition . . . . .	39
4.2.2	Zinc Deposition . . . . .	42
4.3	Convection Effects . . . . .	51
4.3.1	Theoretical Model . . . . .	51
4.3.2	Experimental Observation . . . . .	61
4.4	Comparison of Zinc and Copper Channel Growth . . . . .	64
4.5	Electrokinetic Effects . . . . .	67
4.5.1	Theoretical Model . . . . .	67
4.5.2	Numerical Procedure and Results . . . . .	69
4.6	Effects of Ohmic Heating . . . . .	72
4.6.1	Adiabatic Cells . . . . .	72

	vii
4.6.2 Discussion . . . . .	75
4.6.3 Effect of Ohmic Heating on Concentration Measurements . . . . .	77
4.7 Comparison with Velocity Selection Theories . . . . .	78
4.7.1 Diffusion Controlled Growth Crystal . . . . .	78
4.7.2 Ohmic Controlled Growth Crystal . . . . .	81
<b>5 Conclusions and Recommendations</b>	<b>84</b>
<b>A Interferometric Study of the Concentration Profile</b>	<b>87</b>
A.1 Introduction . . . . .	87
A.1.1 Conventional Laser Interferometry . . . . .	87
A.1.2 Holographic Interferometry . . . . .	89
A.1.3 Digital Phase-Shifted Interferometry . . . . .	90
A.2 Principles of Digital Phase-Shifted Interferometry . . . . .	91
A.2.1 Theory of Interference . . . . .	91
A.2.2 Phase-Shifted Interferometry . . . . .	92
A.2.3 Phase Change Computation . . . . .	93
A.2.4 Electrolyte Concentration Calculation . . . . .	95
A.2.5 Light Deflection Errors . . . . .	96
<b>Nomenclature</b>	<b>97</b>
<b>Bibliography</b>	<b>100</b>

# List of Figures

2.1	Morphology selection (a) Dendrite growth, (b) Tip-splitting growth, (c) dense-branching morphology (DBM) and (d) Channel growth. . . . .	5
2.2	Dendrite morphologies for (a) pivalic acid (PVA) and (b) succinonitrile (SCN). (after Glicksman [10]) . . . . .	8
2.3	Morphologies observed in anisotropic Hele-Shaw cells. (a) ruled channels with fourfold symmetries and (b) ruled channels with a random array on the bottom plate. (after Ben-Jacob [21]) . . . . .	11
2.4	Phase diagram of morphologies for zinc electrodeposition showing the various type of patterns observed as a function of electrolyte concentration and applied voltage. . . . .	16
2.5	Observation of the fluid motion in typical conditions (cell dimensions $1\text{cm} \times 1\text{cm} \times 0.1\text{cm}$ , $0.05\text{M } CuSO_4$ , voltage $5\text{ V}$ ). (after Fleury [43]). . . . .	17
3.1	A Schematic overview of Experimental Setup. . . . .	21
3.2	Schematic of Electrolysis Cells. . . . .	22
3.3	Digital Phase-Shifted Mach-Zehnder Interferometer. . . . .	28
3.4	Concentration profile at 50 seconds for galvanostatic deposition from $0.8\text{M } CuSO_4$ in vertical cell. current density: $40\text{ mA/cm}^2$ . The theoretical curves were computed with Equation 3.11 for current efficiencies of 100% and 75%. . . . .	30
4.1	Morphology from $CuSO_4$ deposition in horizontal circular cells. anode diameter: $25\text{ mm}$ , cathode diameter: $1.0\text{ mm}$ and cell thickness: $250\text{ }\mu\text{m}$ . . . . .	32

4.2	Channel growth of copper from 0.1M $CuSO_4$ at 30 V in a parallel cell. distance between two electrodes: 10 mm, cell thickness: 100 $\mu m$ . . . . .	33
4.3	Dendritic growth of copper from 1M $CuCl_2$ with supporting $HCl$ at 1.4 V in a three-dimensional cell. distance between two electrodes: 10 mm. . . . .	33
4.4	Morphology from $ZnSO_4$ deposition in horizontal circular cells. anode di- ameter: 25 mm, cathode diameter: 1.0 mm and cell thickness: 250 $\mu m$ . . .	36
4.5	Mophology produced by deposition from 0.04M $ZnSO_4$ at 30 V in horizon- tal and vertical parallel cells. cell thickness: 100 $\mu m$ , distance between two electrodes: 30mm . . . . .	38
4.6	Channel growth from deposition from 0.02M $ZnSO_4$ at 35 V in horizontal parallel cell. cell thickness: 100 $\mu m$ , distance between two electrodes: 30mm	39
4.7	Gray-scale image and concentration profile during deposition from 0.05M $CuSO_4$ at 25 V in horizontal parallel cell. cell thickness: 250 $\mu m$ , distance between two electrodes: 30 mm. . . . .	43
4.8	Gray-scale images during deposition from 0.2M $CuSO_4$ at 15 V and 30 V in horizontal parallel cell. cell thickness: 250 $\mu m$ , distance between two electrodes: 20 mm, image frame: 5990 $\mu m \times 3872\mu m$ . . . . .	44
4.9	Gray-scale images during deposition from 0.4M $CuSO_4$ at 15 V and 30 V in horizontal parallel cell. cell thickness: 250 $\mu m$ , distance between two electrodes: 20 mm, image frame: 5990 $\mu m \times 3872\mu m$ . . . . .	45
4.10	Concentration profiles during deposition from $CuSO_4$ in horizontal circular and parallel cells. circular cell: anode diameter = 25 mm, cathode diameter = 1.0 mm, cell thickness = 250 $\mu m$ . parallel cell: distance between two electrodes = 20 mm, cell thickness = 250 $\mu m$ . . . . .	46
4.11	Gray-scale images during deposition from 0.1M $CuSO_4$ at 20 V in horizon- tal and vertical parallel cell. cell thickness: 100 $\mu m$ , distance between two electrodes: 10 mm. . . . .	47

4.12	Gray-scale images during deposition from 0.1M $CuSO_4$ at 13 V in horizontal and vertical parallel cell. cell thickness: 100 $\mu m$ , distance between two electrodes: 10 mm. . . . .	48
4.13	Gray-scale images during deposition from 0.1M $CuSO_4$ at 20 V in horizontal parallel cell. cell thickness: 250 $\mu m$ , distance between two electrodes: 10 mm, image frame: 7747 $\mu m$ $\times$ 6087 $\mu m$ . . . . .	49
4.14	Concentration profiles during deposition from 0.1M $CuSO_4$ at 20 V in horizontal and vertical parallel cells. distance between two electrodes = 10 mm, cell thickness = 100 or 250 $\mu m$ . . . . .	49
4.15	Concentration profiles during deposition from 0.1M $CuSO_4$ at 13 V in horizontal and vertical parallel cells. distance between two electrodes = 10 mm, cell thickness = 100 $\mu m$ . . . . .	50
4.16	Concentration profile normal to the growth direction in between two branches during deposition from 0.1M $CuSO_4$ at 13 V in horizontal parallel cells. cell thickness: 100 $\mu m$ , distance between two electrodes: 10 mm. . . . .	50
4.17	Gray-scale image and concentration profile during deposition from 0.2M $ZnSO_4$ at 25 V in horizontal circular cell. anode diameter = 25 mm, cathode diameter = 1.0 mm, cell thickness = 250 $\mu m$ . . . . .	52
4.18	Gray-scale images during deposition from 0.3M $ZnSO_4$ at 8 V in horizontal and vertical parallel cell. cell thickness: 100 $\mu m$ , distance between two electrodes: 10 mm. . . . .	53
4.19	Gray-scale image and concentration profile during deposition from 0.02M $ZnSO_4$ at 35 V in horizontal parallel cell. cell thickness: 100 $\mu m$ , distance between two electrodes: 30 mm. . . . .	54
4.20	Gray-scale images during deposition from 0.04M $ZnSO_4$ at 30 V in horizontal and vertical parallel cells. cell thickness: 100 $\mu m$ , distance between two electrodes: 30 mm. . . . .	55

4.21	Concentration profiles during deposition from 0.04M $ZnSO_4$ at 30 V in horizontal and vertical parallel cell. distance between two electrodes = 30 mm, cell thickness = 100 $\mu m$ . . . . .	56
4.22	Concentration profiles during deposition from 0.3M $ZnSO_4$ at 8 V in horizontal and vertical parallel cell. distance between two electrodes = 10 mm, cell thickness = 100 $\mu m$ . . . . .	56
4.23	Gray-scale image and concentration profile during deposition from 0.1M $ZnSO_4$ at 42 V in vertical parallel cell. cell thickness: 100 $\mu m$ , distance between two electrodes: 10 mm. . . . .	57
4.24	Demonstration of natural convection observed in copper or zinc deposition from $CuSO_4$ or $ZnSO_4$ in circular and parallel cell with the thickness of 790 $\mu m$ . . . . .	61
4.25	Gray-scale image and concentration profile during deposition from 0.2M $CuSO_4$ at 15 V in vertical parallel cell. cell thickness: 100 $\mu m$ , distance between two electrodes: 30 mm. . . . .	63
4.26	Channel growth in deposition from $ZnSO_4$ and $CuSO_4$ in horizontal parallel cells. cell thickness: 100 $\mu m$ , distance between two electrodes: 10mm . . . .	64
4.27	Gray-scale image of channel growth in deposition from 0.2M $CuSO_4$ in a circular cell. anode diameter: 25 mm, cathode diameter: 1.0 mm, cell thickness: 250 $\mu m$ and image frame: 8638 $\mu m \times 6858\mu m$ . . . . .	66
4.28	Schematic of a needle crystal with a parabolic shape. . . . .	68
4.29	Comparison of the electric potential differential acting on a copper and zinc crystal surface in the tangential direction. . . . .	71
4.30	Schematic of a parallel cell to show the ohmic heating model . . . . .	73
4.31	Theoretical results of ohmic heating in an adiabatic cell: ECD of 0.2M $CuSO_4$ ; applied potential 15 V; cell spacing 250 $\mu m$ ; two electrodes 10 mm apart; $C_i = 0.06M$ ; $\delta = 0.06cm$ $i = 25mA$ and $v = 18.3\mu m/s$ . . . . .	76

4.32 Schematic of glass plates and electrolyte solution in a parallel cell. . . . .	76
4.33 Theoretical relationship of crystal tip radius and growth velocity as the function of applied potential. . . . .	81
4.34 Schematic of a 3-dimensional needle crystal. . . . .	83
4.35 Computed tip radius versus dendrite height for insulating and conducting boundary. potential $\Phi = 25mV$ , growth velocity $v = 0.1\mu m/s$ . . . . .	83
A.1 Optical arrangement of Jamin-type interferometer (L: Ne-Ne laser emitter; B: beam expander; $J_1, J_2$ : Jamin plates; C: experimental cell; S: shutter; $L_1, L_2$ : optical lenses; Sc: screen). (after Nagatsutawa [50]) . . . . .	88
A.2 Optical arrangement for holographic interferometry: L, laser; M1, M2, M3, M4, mirror; B, beam splitter; E1, E2, expander; LE1, LE2, lens; S, shutter; C, electrolysis cell; H, hologram; CA, camera. (after Fukunaka [61]) . . . . .	89



# List of Tables

3.1	Electrode configuration for circular and parallel cells. . . . .	25
3.2	Ultrapure and analytical reagent grade chemicals used in this study. . . . .	25
4.1	Summary of the experimental results for $CuSO_4$ deposition. anode diameter: 25 mm, cathode diameter: 1.0 mm, and cell thickness: 250 $\mu m$ . . . . .	34
4.2	Summary of the experimental results for deposition from $ZnSO_4$ in horizontal circular cells. anode diameter: 25 mm, cathode diameter : 1.0 mm and cell thickness: 250 $\mu m$ . . . . .	37
4.3	Summary of experimental results for electrodeposition in parallel cells. $t$ stands for cell thickness in $\mu m$ , $d$ is the distance between two electrodes in mm, hor. = horizontal cell; ver. = vertical cell. . . . .	40
4.4	Channel Growth of $ZnSO_4$ and $CuSO_4$ Deposition in horizontal parallel cells.	65

**ABSTRACT**  
**EXPERIMENTAL AND NUMERICAL STUDIES ON PATTERN**  
**FORMATION IN ELECTROCHEMICAL DEPOSITION**

by

Zhenqiu Liu  
University of New Hampshire, May, 1995

An experimental and theoretical investigation on pattern formation in electrochemical deposition from copper and zinc binary sulfate electrolyte in two dimensional cells was carried out in this study. Aggregates were produced by electrochemical deposition. An interferometric setup was developed to measure the concentration boundary layer around the aggregates produced during growth.

Convection is observed during electrodeposition from binary sulfate solution of zinc and copper with the concentration of 0.04M and higher in horizontal cells. The theoretical and experimental investigation indicates that natural convection is much stronger in a horizontal cell than that in a vertical cell. Channel growth is observed in our experiment for both zinc and copper deposition from binary sulfate solution. Zinc channel growth is produced under conditions where natural convection is suppressed by deposition in a vertical configuration; however, zinc dendrites are observed in a horizontal cell under the same experimental conditions. In contrast to zinc deposition, channel growth from copper deposition is produced in either the horizontal or vertical configuration. Therefore, the role of natural convection is of primary importance in morphological selection for deposition from  $ZnSO_4$ . However, no effect of natural convection is found on pattern selection for deposition from  $CuSO_4$ .

Electrokinetic streaming was identified as a morphology determining process. The pre-

liminary theoretical results show that the electric force acting at the double layer close to the tip of copper aggregates is much larger than is the case with zinc aggregates. The dependence of morphology selection for zinc and copper deposition on the vertical or horizontal configuration of cells is due to the interaction of natural convection and electrokinetic effects.

Theoretical models of velocity selection developed in solidification were translated to the systems of electrochemical deposition. However, numerical simulations based on this theory for both diffusion controlled and the ohmic controlled growth are not consistent with the experimental results.

An adiabatic cell model was developed to quantify the effect of ohmic heating in the deposition experiments. The predicted temperature increases during electrodeposition in two dimensional cells are much higher than the experimental values, indicating that the cells efficiently shed the heat generated by the passage of current. Analysis based on this adiabatic model shows that the errors for the interferometric concentration measurement due to temperature rises are negligible for electrochemical deposition in two dimensional cells at moderate applied potential.

# Chapter 1

## Introduction

### 1.1 Purpose of Study

The last decade has produced significant advances in understanding of growth processes driven far from equilibrium. The present experimental and numerical studies on dendritic and ramified growth in electrochemical deposition (ECD) were undertaken to place ECD in the broader context of driven growth and to apply the latest models from this field. The experimental investigation was focused on the effects of cell configuration, applied electric potential, electrolyte concentration field and convection on the growth pattern and velocity of electrodeposits. These influences were interpreted through general principles of patterned growth.

The formation of patterns in nature shows some generalized properties. Examples of pattern growth include formation of snowflakes, solidification from melts, precipitation from supersaturated solution, fluid injection in Hele-Shaw cells and electrochemical deposition. All of the systems have been shown to exhibit common morphological types, and they apparently obey common laws of patterned growth. However, the electrochemical system is in some ways unique. It can be driven far from equilibrium and can be easily manipulated with the variation of applied potential or cell current. This advantage makes electrochemical deposition a more versatile experimental system than solidification, in which a large degree of undercooling is difficult to achieve.

From a technological viewpoint, dendritic growth in electrochemical deposition has long

been a concern in battery and metal finishing applications. The instability of electrochemical deposition must be controlled in recharging secondary batteries and in electroplating metal surfaces. For this reason, metals of technological and commercial importance were used in this study. The control parameters (concentration etc.) are typical design parameters for practical systems.

## 1.2 Outstanding Issues

### 1.2.1 Velocity and Morphology of Growth

Pattern formation has been an active subject in physics<sup>[1, 2, 3]</sup> in recent decades. How and why a specific growth velocity and pattern are selected for a given set of conditions is still an unanswered question for many growth systems in nature. Recent theoretical models suggest that driving force, transport dynamics and interfacial dynamics combine and compete to produce the diversity of observed morphologies. Studies on electrochemical deposition provide more information and understanding on this diversity. At the same time, analysis of electrodeposition by use of these models provides insight into the dynamics of ECD.

### 1.2.2 Role of Electrochemistry

The differences between electrochemical deposition and other pattern formation systems has not been given much attention until recent years<sup>[34],[44]--[50]</sup>. The electrochemical system is more complicated, and pattern formation is determined to some extent by the combined effects of electrochemical kinetics, natural and electrokinetic convection and the double layer charge (electrokinetic convection refers to the hydrodynamic flow caused by the interaction of an external electric field and the diffuse double layer near the surface of an electrode). These electrochemical effects are investigated in this study. In particular, we seek to fit these unique effects within the generalized models of pattern formation.

### 1.2.3 Role of Convection

The role of convection in pattern formation has only been investigated recently [44]. The interaction of natural convection and electrokinetic convection in electrochemical deposition leads to various morphology selections. Both natural and electrokinetic convection are determined by the experimental conditions, while electrokinetic convection is strongly related to the electric field applied to the electrolysis cell. We attempted to damp the natural convection with thin two dimensional electrolysis cells in vertical configuration to investigate the electrokinetic convection effects on pattern selection. A theoretical model is applied to estimate the interaction of natural and electrokinetic convection, and their effects on pattern selection.

# Chapter 2

## Literature Review

The formation of patterns was critically reviewed by Langer in 1980 [1], Kessler in 1988 [2] and Brener and Mel'nikov in 1991 [3]. The term "pattern formation" can be applied to an extremely wide variety of disciplines. Extensive experimental and theoretical studies on solidification from melts, precipitation from supersaturated solution, viscous fingering in Hele-Shaw cells, amorphous annealing and electrochemical deposition have been published in the last decade [6]--[50].

### 2.1 Definition of Morphology Selection

The definitions used in this thesis are the same as those used in physics literature on morphology selection to describe the structure of patterns. These concepts apply to any specific system of pattern formation.

**A dendrite** is a branch with a central trunk and sidebranches as showed in Figure 2.1 (a).

As an individual dendrite grows, the tip of the needle crystal retains its integrity in a frame of reference moving with the tip, and sidebranches propagate down the trunk, away from the tip.

**Tip-splitting growth** refers to a pattern formed by the repeated splitting of the tip point of a branch (Figure 2.1 (b)). There is no predominant "trunk" growing in tip-splitting patterns, instead, tips are randomly split into more tips. For diffusion-controlled systems, a special tip-splitting pattern known as dense-branching morphology (DBM),

is often obtained as shown in Figure 2.1 (c). The term DBM refers to the global organization of many branches into a compact aggregate.

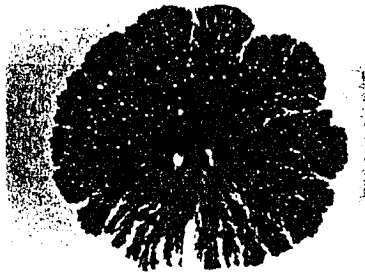
**Channel growth** refers to the pattern growth found in electrochemical deposition in which the branches grows parallel at the same velocity without sidebranching as the teeth in a comb (Figure 2.1 (d)). The branches are very thin in comparison with the overall size of the aggregates in channel growth.



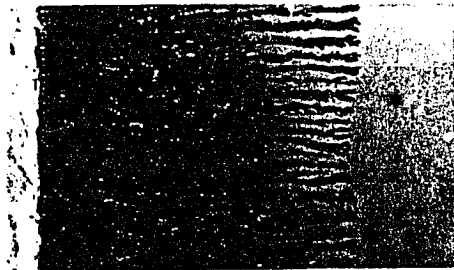
(a)



(b)



(c)



(d)

Figure 2.1: Morphology selection (a) Dendrite growth, (b) Tip-splitting growth, (c) dense-branching morphology (DBM) and (d) Channel growth.

Similar patterns are classified into the same categories even if they are generated from different systems, and the length scales can be quite different. For example, dendrites



of decimeters in length can be formed in the anisotropic Hele-Shaw cell [21] when air is driven to replace the glycerin in the cell; dendrites of centimeters in length can be produced by electrodeposition of zinc from concentrated  $ZnSO_4$  [34]; and dendrites of microns in length are obtained by solidification from the melt or precipitation from supersaturated solutions [16, 15]. Tip-splitting patterns on the decimeter scale are produced in the isotropic Hele-Shaw cell [21]; centimeter scale tip-splitting growth is observed in ECD of copper [34], and micron scale tip-splitting patterns occur in the annealing of amorphous aluminum germanium [18]. Channel growth has been only reported on the centimeter scale in ECD from dilute  $ZnSO_4$  at high cell potential [42].

## 2.2 Dendritic Growth in Solidification

Crystal dendrites can be produced by precipitation from supersaturated solution or solidification of the subcooled melt. The instability of a crystallization interface, analysed by Mullins and Sekerka [4, 5], results in the development of dendritic trunks. Secondary instability gives rise to the growth of side branches on initially parabolic dendrites. Mullins and Sekerka treated directional solidification in which a one dimensional front advances into a subcooled melt at a controlled velocity.

### 2.2.1 Theoretical Model

For the solidification of a pure substance from its melt, the process is governed by heat flow [1, 2]. The rate of solidification at any point along the liquid-solid interface depends on the rate of latent heat generated at that point being conducted into the bulk of the liquid at the boundaries. The temperature field satisfies the thermal diffusion equation in the form

$$\frac{\partial T}{\partial t} = D_T \nabla^2 T \quad (2.1)$$

where  $D_T$  is the thermal diffusion constant. Two equations in the form of Equation 2.1 are

required, one for the solid phase with the solid thermal diffusion constant  $\acute{D}_T$ , and another for the liquid phase with the liquid thermal diffusion constant  $D_T$ .

The condition of heat conservation at a point on the moving interface is given as

$$Lv_n = [\acute{D}_T \acute{c}_p \cdot (\nabla T)_{solid} - D_T c_p \cdot (\nabla T)_{liquid}] \cdot \hat{n} \quad (2.2)$$

where the left-hand side is the rate at which heat is generated at the boundary, and the right-hand side is the rate at which this heat flows into the bulk phases on either side. Here  $L$  is the latent heat per unit volume of the solid;  $v_n$  is the normal velocity of the interface growth;  $c_p$  is the heat capacity per unit volume; and  $\hat{n}$  is the unit normal at the interface from solid into liquid; primed symbols denote the properties of the solid phase and unprimed symbols denote those of the liquid.

The microscopic interfacial dynamic condition includes the contribution of surface tension and surface kinetics. If the undercooling at the interface due to surface tension obeys the Gibbs-Thomson relation and the kinetic undercooling is proportional to the normal growth velocity  $v_n$

$$T_{interface} = T_M - \left(\frac{L}{c_p}\right) d_0 \kappa - \left(\frac{L}{c_p}\right) \beta_0 v_n \quad (2.3)$$

where  $T_M$  is the melting temperature,  $d_0$  is the capillary length which is proportional to the liquid-solid surface tension,  $\kappa$  is the curvature of the interface, and  $\beta_0$  is a kinetic factor.

Equations 2.1, 2.2 and 2.3 completely specify the model of solidification of a pure substance. Convection in the fluid is ignored, and crystalline anisotropy is not included in the model. Even with these simplifications, this free-boundary problem is complicated for numerical solution.

### 2.2.2 Experimental Studies

Solidification from camphene, succinonitrile (SCN), pivalic acid (PVA) and other organic melts have been extensively investigated by Glicksman and coworkers [6]--[15]. Typical dendritic growth patterns are shown in Figure 2.2 [10]. The principal growth characteristics of the dendrites are a nearly constant velocity and a smooth tip with evenly spaced side branches. Experimental investigation of succinonitrile solidification by Glicksman and coworkers was the first experiment in which the tip radius and growth velocity were measured. This allowed them to test various steady-state theories of velocity selection.

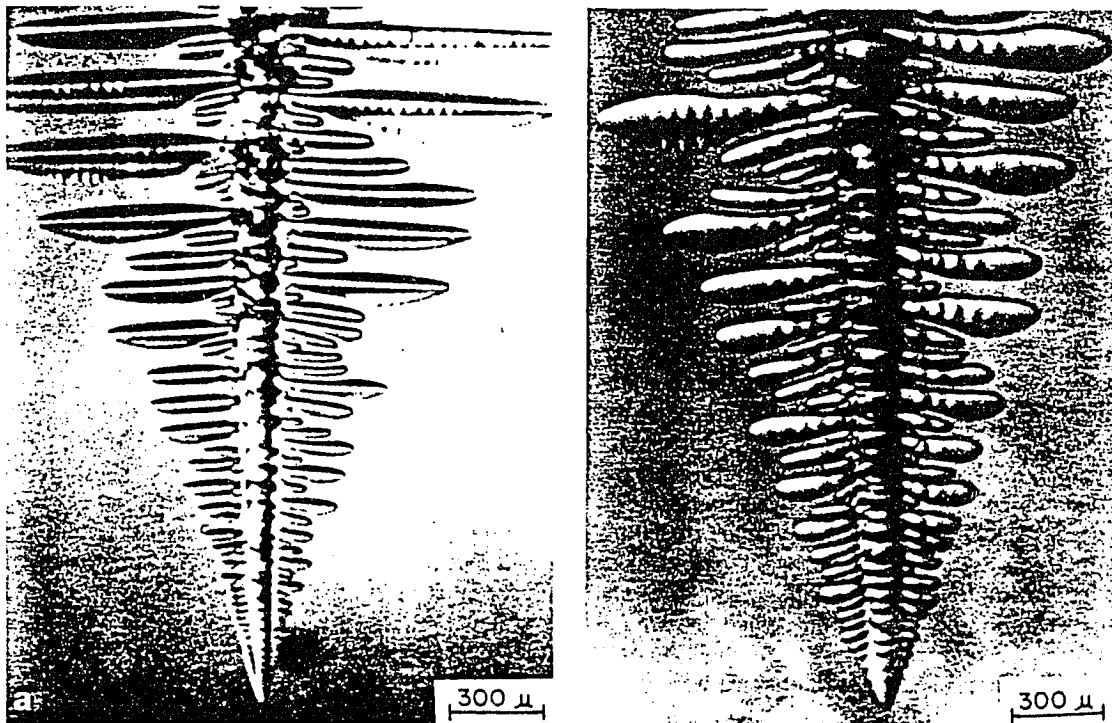


Figure 2.2: Dendrite morphologies for (a) pivalic acid (PVA) and (b) succinonitrile (SCN). (after Glicksman [10])

Their results showed that the relation between the degree of supercooling and growth velocity and tip radius is consistent with the marginal stability theory for some of the

materials they studied, but deviates from the maximum velocity predictions by factors of 5 or more in both tip radius and growth velocity. Their data did not support “microscopic solvability” theory, in which the growth velocity is a function of the supercooling multiplied by the surface tension anisotropy to the 7/4 power [6]. They have studied the effects of free convection in solidification and shown that free convection is often significant, especially for less viscous melts and low driving force.

## 2.3 Pattern Formation in Hele-Shaw Cells

The Hele-Shaw cell provides a simple means of studying pattern formation. It consists of two closely placed plexiglass plates with a layer of viscous fluid between them. A structure interface is formed when a less viscous fluid is injected to displace a more viscous one in the cell. Both DBM and dendritic growth are observed due to interfacial instability. [19, 20, 21]

### 2.3.1 Theoretical Model

Assuming no-slip boundary conditions along the top and bottom plates, for low Reynolds number, the velocity in a Hele-Shaw cell obeys Darcy’s law [17]

$$\vec{V} = -\frac{b^2}{12\mu}\nabla p \quad (2.4)$$

where  $b$  is the gap between two plates,  $\mu$  is the fluid dynamic viscosity, and  $p$  is the pressure.

For an incompressible fluid,  $\nabla \cdot \vec{V} = 0$ , and Darcy’s law becomes

$$\nabla^2 p = 0 \quad (2.5)$$

At the interface of two fluids, conservation of mass requires the phase boundary to move at the local fluid velocity for immiscible fluids, thus

$$-\vec{n} \cdot \nabla p = \frac{12\mu}{b^2} v_n \quad (2.6)$$

where  $\vec{n}$  is a unit normal and  $v_n$  is the normal growth velocity of the interface.

With surface tension and a kinetic overpressure across the interface, the pressure along the interface is given by [21]

$$p_i = p_a - d_0 \kappa - \beta_0 v_n^\gamma \quad (2.7)$$

where  $p_i$  and  $p_a$  are the pressure at the interface and applied pressure, respectively.  $d_0$  is the capillary length which is proportional to the surface tension,  $\kappa$  is the curvature of the interface, and  $\beta_0$  and  $\gamma$  are kinetic parameters.

Ben-Jacob and Garik [21] introduced anisotropy into their two-dimensional model in which  $d_0$  in Equation 2.7 is replaced by

$$d_0[1 - d_1 \cos(m\theta)]$$

where  $d_1$  is the magnitude of the  $m$ -fold anisotropy and  $\theta$  is the angle between some fixed direction in space and the direction normal to the interface.

### 2.3.2 Experimental Studies

Ben-Jacob and coworkers [19, 20, 21] investigated pattern formation in Hele-Shaw cells, in which ruled channels were cut on the bottom plate to provide anisotropy with fourfold symmetries or a random array as shown in Figure 2.3. Dendritic growth patterns resembling snowflakes were observed when the bottom plates of the cells were ruled with symmetric channel cuts (Figure 2.3 (a)), while tip-splitting growth occurred for cell bottoms with random cuts (Figure 2.3 (b)).

These experiments as well as numerical simulations led them to the hypothesis that

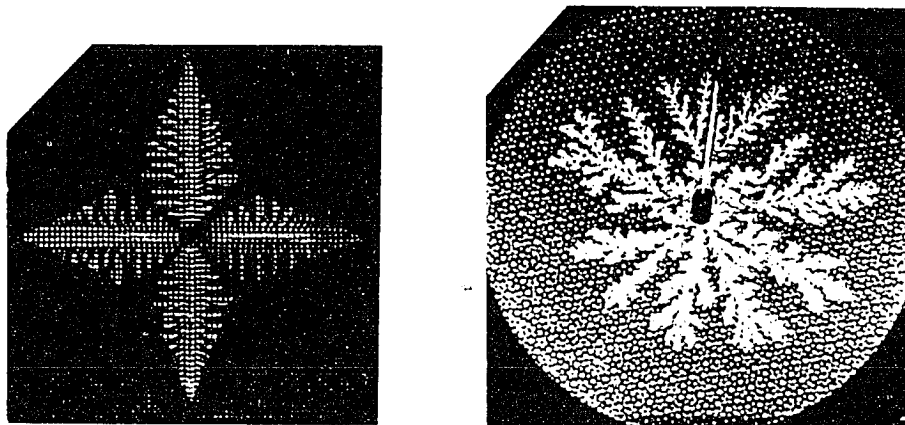


Figure 2.3: Morphologies observed in anisotropic Hele-Shaw cells. (a) ruled channels with fourfold symmetries and (b) ruled channels with a random array on the bottom plate. (after Ben-Jacob [21])

interfacial anisotropy stabilized dendrites against tip-splittings. They argue that in the case of solidification, there is a temperature gradient along the surface of the dendrite since the melting temperature depends on curvature. As a result, energy flows towards the tip. This warming slows the advance of the tip, while the corresponding cooling of points at the sides near the tip causes these points to advance faster and to overtake the tip. This interfacial heat balance dynamic probably accounts for tip-splitting growth. For dendrites to form, the anisotropy must be large enough to suppress the heat flow towards the tip so that the tip will be no longer the coldest point along the interface. A needle crystal with a particular tip velocity and tip radius will have its coldest point, as determined by a balance between curvature and crystalline orientation, at a distance from the tip. The instability is then propagated away from the tip.

## 2.4 Electrochemical Deposition

Electrochemical deposition can produce patterns indistinguishable to the eye from those arising in non-equilibrium crystal growth or instability patterns from Hele-Shaw cell exper-

iment.

In recent years, studies on electrodeposition have become important because they offer the possibility of a wide variety of aggregation conditions with relatively easily manipulated experimental parameters [34]. Experimental and theoretical studies on electrodeposition of zinc and copper with emphasis on morphology dependence on experimental conditions have been reported [33]--[50].

### 2.4.1 Theory of Electrochemical Deposition

The flux of each specie in an electrolytic solution is governed by the transport equation, which accounts for the contribution of migration, diffusion and convection in the form [69]

$$\vec{N}_i = -z_i u_i F c_i \nabla \Phi - D_i \nabla C_i + C_i \vec{v} \quad (2.8)$$

Flux  $\vec{N}_i$  of species  $i$  is caused by the motion of the fluid with the bulk velocity  $\vec{v}$ , as well as diffusion if there is a concentration gradient  $\nabla C_i$  and migration if there is an electric field  $-\nabla \Phi$ .  $z_i$  is the number of proton charges carried by an ion,  $u_i$  is an ion mobility and  $F$  is the Faraday constant.

The material balance for component  $i$  in a cell without homogeneous chemical reaction is

$$\frac{\partial C_i}{\partial t} = -\nabla \cdot \vec{N}_i \quad (2.9)$$

In the bulk, Poisson's law can be used

$$\nabla^2 \Phi = \frac{F}{\epsilon} \sum z_i C_i \quad (2.10)$$

where  $\epsilon$  is the dielectric constant.

The above equations must be supplemented by boundary conditions at the aggregate-

electrolyte interface. Applying conservation of mass at the interface and assuming that only component 1 is electroactive, we have

$$\vec{n} \cdot \vec{N}_1 = \frac{t \cdot i_n}{zF} \quad (2.11)$$

where  $t$  is the ion transference number and  $i_n$  is the normal current density. For other components ( $i \neq 1$ ), we have

$$\vec{n} \cdot \vec{N}_i = 0 \quad (2.12)$$

One more boundary condition is needed to complete this system of equations. The condition must be related to the kinetics of the charge transfer reaction taking place at the interface. Local thermodynamic equilibrium is assumed in the case of solidification; in electrochemical deposition, non-equilibrium kinetics are important. The Butler-Volmer equation describes the kinetics of an electrode where the exchange current density  $i_o$ , an electrochemical rate constant, is depends on the reactant concentration

$$i_n = i_o \left[ \exp\left(\frac{\alpha_a F}{RT} \eta_s\right) - \exp\left(-\frac{\alpha_c F}{RT} \eta_s\right) \right] \quad (2.13)$$

This expression relates the surface overpotential  $\eta_s$  to the normal current density  $i_n$ ; the exchange current density  $i_o$  and the transfer coefficients  $\alpha_a$  and  $\alpha_c$  can be obtained from experimental data.

Bockris and Reddy <sup>[51]</sup> introduced the idea of modified equilibrium potential drop  $\Delta\phi_e$  to include the effects of surface energy. The surface overpotential in Butler-Volmer equation can be expressed by

$$\eta_s = \Delta\phi - \Delta\phi_e \quad (2.14)$$

where the equilibrium potential drop  $\Delta\phi_e$  is given as



$$\Delta\phi_e = \Delta\phi_e^o - \frac{\gamma\kappa V_m}{ne} \quad (2.15)$$

$\Delta\phi_e^o$  is the equilibrium potential drop for a flat surface,  $\gamma$  is the surface tension,  $\kappa$  is the curvature of the interface,  $V_m$  is the molar volume and  $e$  is the charge of an electron.

The concentration gradient of the reacting species in a thin layer near the electrode causes an additional overpotential, which can be approximated by [52]

$$\eta_{cn} = \frac{RT}{nF} \ln(1 - i/i_l) \quad (2.16)$$

where  $i_l$ , the limiting current density, is the maximum current density at which a diffusion limited electrode reaction can proceed. At a higher current density some other electrode reaction will also occur. The total overpotential,  $\eta$ , which comprises surface overpotential and concentration overpotential, is defined by

$$\eta = V - \Phi \quad (2.17)$$

where  $V$  is the applied potential and  $\Phi$  is the potential adjacent to the electrode surface.

The overpotential in Equation 2.17 is obtained from Equation 2.13 and Equation 2.16, which are nonlinear. For the primary current distribution the overpotential in Equation 2.17 is zero and  $\Phi = V$ .

Anisotropic interfacial conditions for ECD can be included in the mathematical model as in the case of Hele-Shaw cells. These would appear as an angular variation of  $\gamma$  and  $i_o$ . However, this is much more complicated in electrochemical deposition because electrokinetic convection, double layer charging and ohmic heating can be important under certain experiment conditions.

### 2.4.2 Experimental and Theoretical Studies

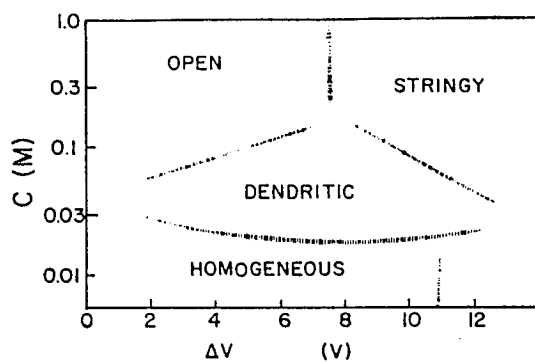
Experimental studies on electrodeposition of zinc from aqueous solutions of  $ZnSO_4$  in radial two-dimensional cells were reported by Sawada and coworkers [37, 38], and Grier and coworkers [39]. Sagues and coworkers [40, 42] studied the electrodeposition of zinc in parallel two-dimensional cells and found that the morphologies depended on electrolyte concentrations and applied cell potentials in a similar manner to that of the radial cells [37] (see Figure 2.4).

The boundaries shown in the phase diagrams depend to some extent on the cell thickness and the temperature [37]. The effects of cell thickness and forced convection of electrolyte on pattern selection had also been investigated [42].

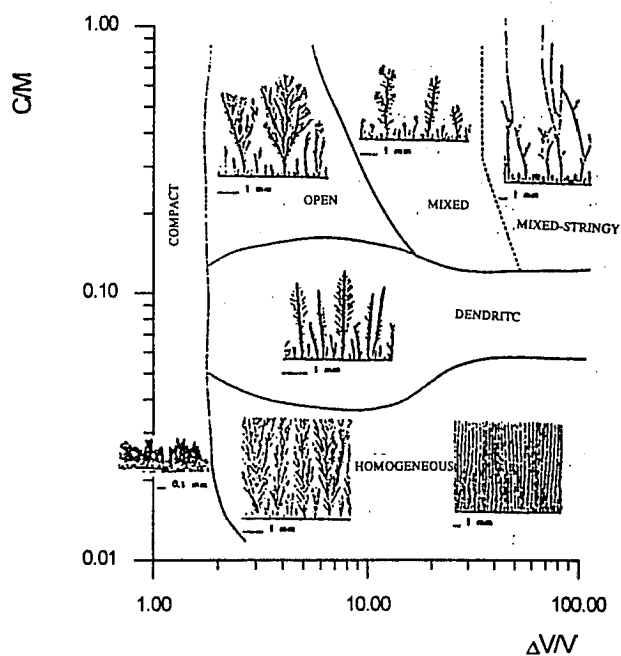
Barkey and coworkers [33, 34, 36] studied the electrodeposition of copper and zinc from binary aqueous electrolyte of  $CuSO_4$  and  $ZnSO_4$ . Smooth concentration envelopes were observed around the aggregates formed by electrodeposition. A theoretical model based on the material balance at the growth front was presented [34] with the assumptions that the aggregate can be treated as a homogeneous disk filling the space between plates and that its electrical resistance is negligible. The predicted growth velocity was in good agreement with experimental data from ECD from  $CuSO_4$  solution in a circular cell. They found that the electrodeposition takes place at the limiting current so that the concentration of electrolyte vanishes at the surface of the aggregates.

Experimental and theoretical studies on electrodeposition of copper from aqueous solutions of  $CuSO_4$  were reported by Fleury and coworkers [44]–[49]. They made the fluid motion visible by means of adding small droplets of oil in the aqueous  $CuSO_4$  solution as shown in Figure 2.5.

In their theoretical model [48, 43], they assume that there exist two zones: Zone I (space charge region) is a layer close to the cathode, where the concentration of anions is neglected, and where only cations exist and, there is therefore an excess of positive charge. Zone II



(a) in radial two-dimensional cells (after Sawada [37]).



(b) in parallel two-dimensional cells (after Sagues [40]).

Figure 2.4: Phase diagram of morphologies for zinc electrodeposition showing the various type of patterns observed as a function of electrolyte concentration and applied voltage.

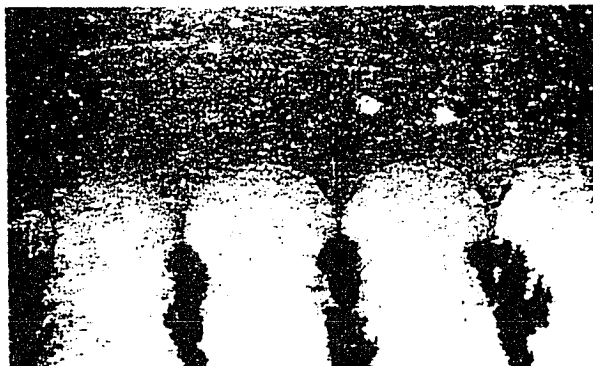


Figure 2.5: Observation of the fluid motion in typical conditions (cell dimensions  $1\text{cm} \times 1\text{cm} \times 0.1\text{cm}$ ,  $0.05\text{M CuSO}_4$ , voltage  $5\text{ V}$ ). (after Fleury [43]).

(quasineutral region) is a region further from the cathode beyond Zone I and which extends to the anode, where the solution is expected to be quasineutral. The thickness of Zone I is on the order of  $1\text{--}10\ \mu\text{m}$ , and that of Zone II of  $100\ \mu\text{m}$ . The ion flux due to migration, diffusion and electroconvection is also taken into consideration.

They also modeled the fluid mechanics near the deposit to determine the role of electroconvection. They model the deposit as a comb of linear branches evenly spaced across the cell. They further assume that point charges reside on the tips of the two-dimensional comb. Their analytical solution indicates that fluid motion similar to that as shown in Figure 2.5 is obtained. Each tip is fed by a “cone” at the junction of two vortices.

This model may not apply to the growth of needlelike crystalline dendrites, where large vortices between neighboring tips do not exist, and the boundary conditions near the dendrite are clearly not the same as in the rectilinear comb assumption.

They report for example, that the experimental studies of dendritic zinc deposition by Barkey [33] was not represented by their model, because the zinc aggregates obtained at low concentration are too compact and the branches are too close to each other to allow the presence of vortices between them.

Bruinsma and Alexander [50] introduced electrohydrodynamic instability analysis to

electrodeposition. They concluded that electrokinetic convection is small compared to the flow velocity of gravity-driven natural convection under normal experimental conditions (i.e., planar interface). In their model, the condition for electrokinetic convection being dominantly depends only on material parameters of the solvent.

## 2.5 Theory of Velocity Selection

Pattern formation in solidification, Hele-Shaw and electrochemical deposition has many general features, though the physical natures of the processes are very different and sometimes rather complicated. For instance, crystal growth is governed mainly by diffusion of heat and/or impurities from or to the region of a phase transition. Recent studies show that dendritic growth also crucially depends on anisotropic and kinetic effects at the interface. In the Hele-Shaw cell, fingers result from the competition between the pressure gradient that drives the flow and surface tension and friction of fluid against the walls which retard it. Dendrite formation in solidification is governed by temperature field (thermal diffusion) near the liquid-solid interface surface tension and surface kinetics, while the process of dendritic growth in precipitation is controlled by concentration field (chemical diffusion), surface tension and surface kinetics. Aggregate growth in electrochemical deposition depends on the concentration field, electric field acting on a cell, as well as surface tension and surface kinetics of aggregate formation.

The question of velocity selection and the shape of a dendrite is a problem in non-linear dynamics [25]. The steady state solutions of the diffusion equation for a two-dimensional dendritic growth, Ivantsov solution, define a family of parabolic needle crystals and a set of growth velocities for a given driving force or undercooling. The tip radius is inversely proportional to the growth velocity for a given undercooling. The Ivantsov solution assumes equilibrium at the growth interface and neglects surface tension.

Langer and Muller-Krumbhaar [22, 23, 24] introduced the marginal stability hypothesis

to modify the Ivantsov solution with the introduction of surface tension as a perturbation. The overall agreement between theory and experimental data from solidification of succinonitrile (SCN) and pivalic acid (PVA) melts by Glicksman and coworkers [6]--[15] provides strong support for the stability hypothesis. However, this theory is not adequate to describe highly anisotropic systems, where anisotropy must be included in both the steady-state calculation and the stability analysis.

An important breakthrough in the problem of dendritic growth was achieved with the introduction of the "microscopic solvability criterion" independently by Kessler and coworkers [26, 27], and Ben-Jacob and coworkers [28, 29, 30]. Kessler and coworkers developed a simplified local model, while Ben-Jacob and coworkers introduced the boundary-layer model. Their results can be summarized as follows:

- no steady-state solutions are obtained when even a very small isotropic surface tension is assumed in the model;
- by introduction of anisotropic surface tension in the boundary condition, a discrete set of allowed growth velocities is obtained;
- only the marginally stable solution corresponding to the maximum growth velocity is observed.

Analytical and numerical methods have been developed to calculate the selected velocity in the limit of small undercooling and small anisotropy for solidification [2, 31]. Good agreement has been achieved with time-dependent supercomputer simulations of the full solidification problem [32], however, this selection hypothesis has not yet been supported by experiment.

Due to the much more complicated physics involved in the mechanism of sidebranching, no theoretical model has been successfully developed on this subject.

# Chapter 3

## Experimental

### 3.1 Electrochemical Deposition

Experimental studies on electrochemical deposition were carried out in quasi two-dimensional cells. In two-dimensional cells, theoretical studies on ECD are much simpler, and observation of growth patterns and measurement of growth velocity is much easier. Furthermore, free convection can be damped to some extent in a two-dimensional cell with thin spacings.

Glass plates are used because they are transparent, nonporous and sufficiently cleanable to form a contamination-free two-dimensional cell. Many experimental studies on ECD have been carried out in plexiglass cells, and the electrolytes were certainly contaminated with leachates from the plastic. Since a slightly contaminated environment may destroy crystal growth, great efforts must be made to ensure purity in ECD experiments.

#### 3.1.1 Experimental Setup Overview

The experimental setup for this study is shown in Figure 3.1. Electrochemical deposition is driven in an electrolysis cell by a Potentiostat/Galvenostat (PARC Model 362 or 273) or filtered D.C. Power Supply (EPSCO Model NFB). Potential and current data are recorded either by a host computer or a strip chart recorder. The deposition process was observed and photographed with a Photo-Microscope (Wild Model 420) equipped with a 35 mm reflex camera.

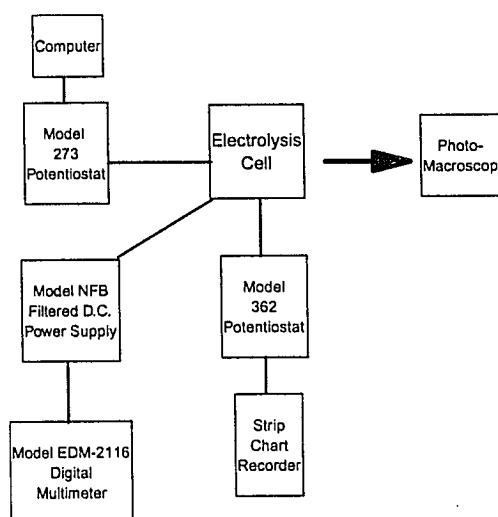


Figure 3.1: A Schematic overview of Experimental Setup.

### 3.1.2 Apparatus and Materials

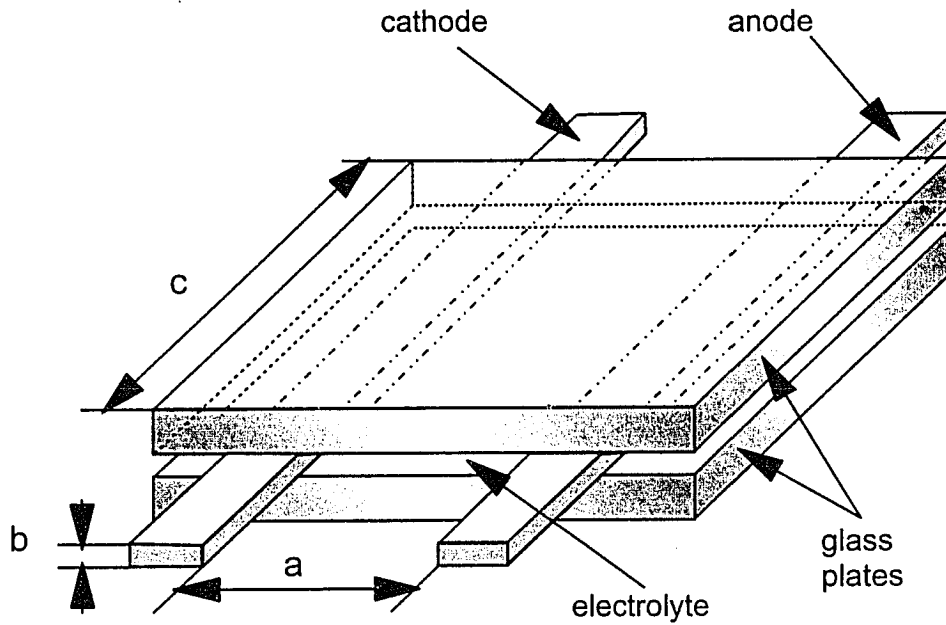
#### Electrolysis Cells

Electrolysis cells with either parallel or circular electrodes were used in this study. Two square glass plates, 3 inches on a side and one quarter-inch in thickness were used to form a quasi two-dimensional electrolysis cell.

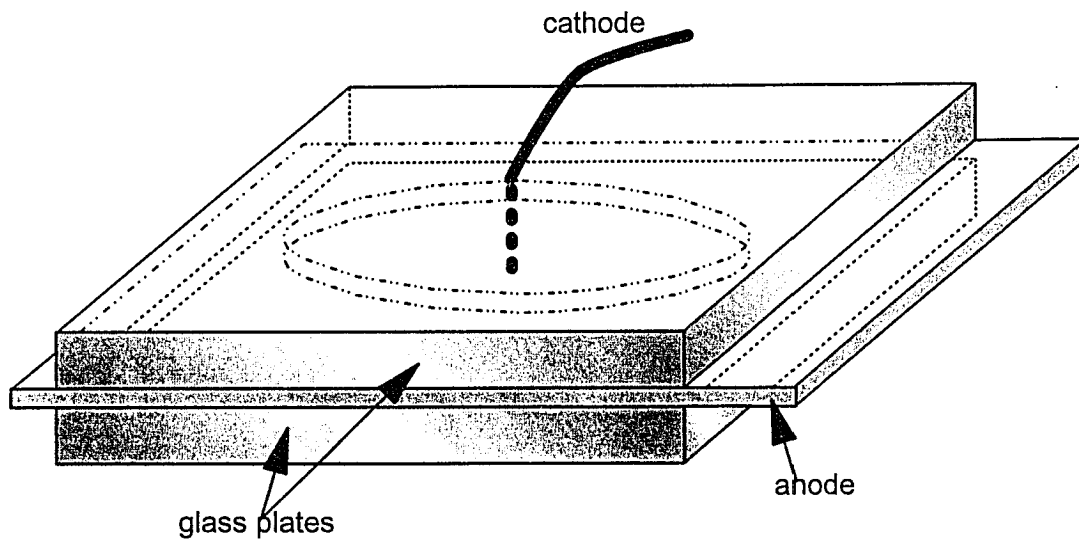
- An electrolysis cell with parallel electrodes consists of two square glass plates, with electrolyte solution sandwiched in between and two parallel metal foil strips of thickness  $50\ \mu\text{m}$ ,  $100\ \mu\text{m}$  or  $250\ \mu\text{m}$  and placed  $10\ \text{mm}$  apart which served both as electrodes and spacers. (See Figure 3.2 (a)).

Parallel cells are chosen for this study since quasi steady state pattern growth is possible in this configuration when galvanostatic control is applied. Parallel cells also provide a simple environment of one-dimensional growth of electrodeposit.





(a) Electrolysis cell with parallel electrodes



(b) Electrolysis cell with circular electrodes

Figure 3.2: Schematic of Electrolysis Cells.

- An electrolysis cell with circular electrodes is shown in Figure 3.2 (b). There is a non-through hole with the diameter of 0.5 *mm* or 1.0 *mm* in the center of the bottom glass plate and a through hole of the same diameter in the center of the upper glass plate. The cathode was a metal wire of 0.5 *mm* or 1.0 *mm* in diameter which goes through the holes from the top glass plate to the bottom glass plate and the anode was a circularly-cut metal foil with the thickness of 100  $\mu\text{m}$ , 250  $\mu\text{m}$  or 790  $\mu\text{m}$  and with a diameter of 25 *mm*.

Electrochemical deposition in radial cells is analogous to growth of crystals where the cathode in the center of the cells acts as the seed acts in crystallization.

### Power Supply for the Electrolysis Cells

Three potentiostats were used. The choice in each case depends on voltage requirement and programmability.

- An EG&G PARC Model 273 Potentiostat/Galvanostat system controlled by a computer (IBM System 2 Model 30 or Model 55 SX) with M342C Corrosion Measurement Software and Head Start Electrochemistry Software installed was used for some of the potentiostatic and galvanostatic electrochemical deposition studies. The equipment and the software were made by EG&G Princeton Applied Research Co. (EG&G PARC). The maximum potential and current for this system were 10 *V* for potentiostatic and 1 *A* for galvanostatic control, respectively. The 273 provides the most versatility in applied wave tracking.
- An EG&G PARC Model 362 Scanning Potentiostat was used for some of the experiments. Potential and current were recorded by a Model BD 41 Strip Chart Recorder made by KIPP&ZONEN, Holland. The potential and current ranges for this system were the same as Model 273 Potentiostat/Galvanostat system.

- A Model NFB FILTERED D.C. POWER SUPPLY made by EPSCO Inc. was used for experiments in which the potential was greater than 10 V for potentiostatic operation. An Escort Model EDM-2116 Digital Multimeter was used to monitor the cell current.

### **Photo/Image Acquisition Facilities**

A Model M420 macroscope with a MINOLTA MAXXUM 7000i camera was used to record images in-situ at magnifications up to 128 $\times$ . The macroscope was made by Wild Heerbrugg Ltd., Switzerland. Fine structure of the deposits could be observed and recorded in photos.

A MINOLTA X-370 camera with a Vivitar 1:1 Macro Telephoto lens was used to photograph the entire cell for some experimental runs. This was useful for recording the overall growth pattern.

After the films or slides were developed, the growth velocity was calculated by measurement of the displacement between consecutive pictures.

### **Ultrapure Water**

Ultrapure water was produced in a Nanopure II Ultrafiltration System. Tap water was first filtered in a carbon black cartridge and an ion exchange cartridge then distilled in a glass distilling apparatus. The distilled water was further purified in a Nanopure II Ultrafiltration System with ion exchange resin and finally filtered with a 0.2  $\mu m$  opening glass fiber filter. The resistivity of the ultrapure water was 17–18  $M\Omega \cdot cm$ . Ultrapure water was used for all rinsing steps and for making solutions.

### **Glass Plates**

All the glass plates for electrolysis cells were purchased from Portland Glass. Square glass plates 3 inches on a side and one quarter-inch in thickness were used.

## Electrodes

Electrodes were made of ultrapure Zinc or Copper (99.998%) which was purchased from Johnson Matthey or Aldrich Chemical Company. Zinc and copper foil were cut to appropriate shapes for electrodes as shown in Table 3.1.

Electrode Dimensions				
Material	Zinc		Copper	
	parallel	circular	parallel	circular
cell type				
thickness ( $\mu m$ )	50, 100, 250	100, 250, 790	100, 250	100, 250
width ( $mm$ )	10	N/A	10	N/A
inner-cut diameter ( $mm$ )	N/A	15, 25	N/A	15, 25
wire diameter for anode ( $mm$ )	N/A	0.5, 1.0	N/A	0.5, 1.0

Table 3.1: Electrode configuration for circular and parallel cells.

## Chemical Reagents

Chemical reagents used in the experiment are listed in Table 3.2. Analytical reagent grade chemicals were first used for preliminary studies, then ultrapure chemicals were used for selected experimental conditions.

Chemical Reagents		
Chemicals	Content of assay (%)	Source
$ZnSO_4 \cdot 7H_2O$	99.5	EM Science
$CuSO_4 \cdot 5H_2O$	99.0	EM Science
$ZnSO_4 \cdot 7H_2O$	99.999	Johnson Matthey
$CuSO_4 \cdot 5H_2O$	99.999	Johnson Matthey
$H_2SO_4$	95.0–98.0	Fisher Scientific
$HNO_3$	69.0–71.0	Fisher Scientific
Nochromix		GODAX Lab Inc.

Table 3.2: Ultrapure and analytical reagent grade chemicals used in this study.

### 3.1.3 Procedures

All materials used for this study were of high quality and extremely pure to ensure no impurity disturbed the aggregate growth. Standard procedures have been developed for cleaning glassware, electrodes and assembling electrolysis cells. Impurity contamination was avoided in glass plates and glassware cleaning, electrodes cleaning, solution making and electrolysis cell assembling in which only Teflon-coated tongs were used and no hand contact was allowed in handling glass plates and electrodes.

#### Cleaning of Glass Plates and Glassware

All the glass plates and glassware used in the experiment were submerged in Nochromix concentrated sulfuric acid cleaning solution for several hours to remove organic contamination and metal, then rinsed in ultrapure water for three times and finally air-dried at room temperature.

#### Preparation and Cleaning of Electrodes

Metal strips for parallel electrodes were cut from  $100\text{mm} \times 100\text{mm}$  Zinc or Copper foil with a paper cutter. The width of each metal strip was of  $10\text{ mm}$ . Two metal strips were glued onto a small piece of plexiglass block to keep them parallel and a fixed distance from each other.

Zinc and Copper electrodes were first dipped in dilute nitric acid solution to wash out any organics and metal oxides, then rinsed in ultrapure water three times and finally air-dried at room temperature.

#### Preparation of Solutions

Extreme care must be taken in weighing chemicals, pouring chemicals into a volumetric flask, dissolving chemical with ultrapure water and adding water to a specific amount to ensure no hand contact or any other possible contamination to the solutions.

## Assembling of Electrolysis Cells

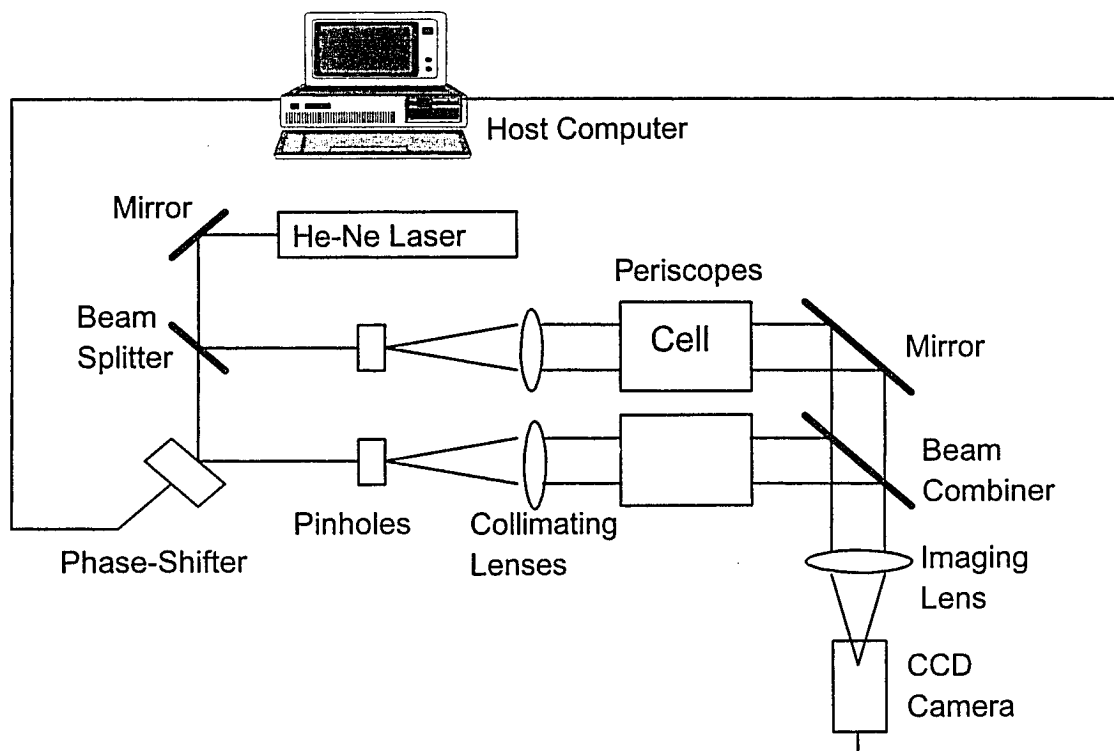
Only clean Teflon-coated tongs were used to handle the glass plates and electrodes while assembling electrolysis cells. A pair of electrodes was put on the top of a glass plate, then electrolyte solution was poured onto the glass plate and another glass plate was put on top of the electrodes with great care to keep the cell clear of air bubbles. The cell was finally tightened with four clamps or with the four bolts in the cell tray.

## 3.2 Interferometry

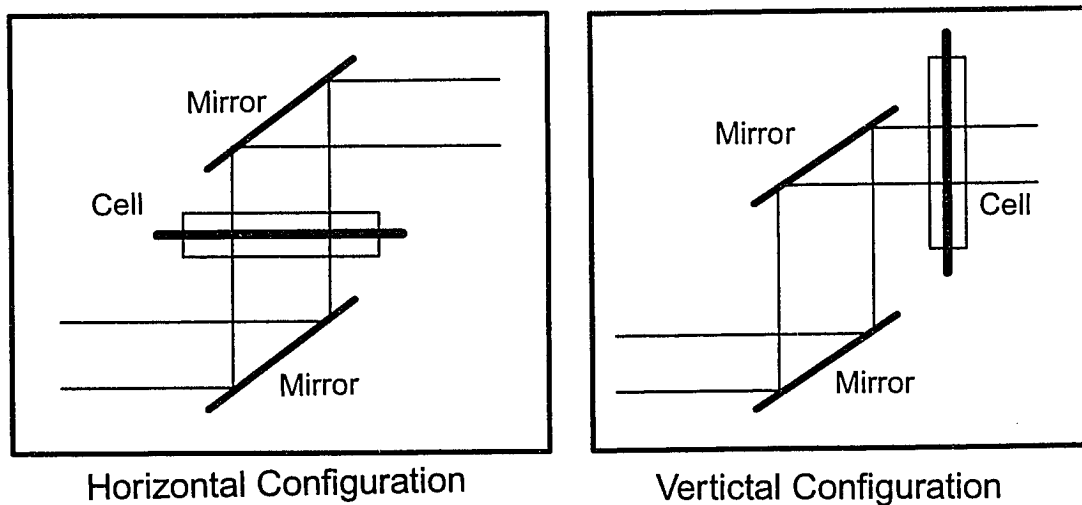
### 3.2.1 Digital Phase-Shifted Mach-Zehnder Interferometer

The Phase-Shifted Mach-Zehnder interferometer is shown schematically in Figure 3.3. The light source is a 5 milliwatt He-Ne laser emitter. The intensity of the light beam from the laser is adjusted through the use of a pair of polarizers. The beam is split into object and reference beams by a beam splitter and each beam is spatially and temporally collimated with a lens and pinhole system. The object beam traverses the electrolysis cell while the reference beam traverses a similar distance of undisturbed air. The object beam is reflected to combine the reference beam by a mirror which is mounted to a translator and can be precisely adjusted without changing the angle of incidence between the object beam and the beam combiner. The object beam and the reference beam impinge on the beam combiner at approximately right angles to one another. The interference pattern is formed on the beam combiner and is focused onto the CCD camera by an imaging lens.

There is no adjustable aperture in the system, and the intensity of the reference and object beams are adjusted through the use of a pair of polarisers. The known phase shifts in the reference beam are produced with a piezo-electric transducer and phase shifting is done on the reference beam before it is collimated.



(a) Overall Schematic



(b) Side view of periscope with cell

Figure 3.3: Digital Phase-Shifted Mach-Zehnder Interferometer.

### 3.2.2 Magnification

A RMB miniature bearing with the diameter of  $\frac{1}{8}$  inch is used for calibration of the magnification of the optical apparatus. The bearing was put on the electrolysis cell, and the image with the bearing was taken and recorded in the host computer. The number of pixels that the bearing occupied in the image in both  $x$  and  $y$  direction was given in the imaging scanning subroutine. The magnification was the actual diameter of the bearing ( $\frac{1}{8}$  inch) divided by the number of pixel in  $x$  or  $y$  direction which the bearing occupied.

The magnification for the experimental runs ranged from  $6.5 \mu m/pixel$  to  $15 \mu m/pixel$ .

### 3.2.3 Velocity of Aggregate Growth

The actual length of the aggregates at any instant could be computed from the image taken during aggregate growth. The velocity could also be obtained from the length of the aggregates measured between two consecutive timed exposures.

### 3.2.4 Accuracy of the Concentration Measurement

The reliability of the interferometric setup for concentration measurement was tested by galvanostatic deposition at low cell current from concentrated 0.8M  $CuSO_4$  solution in the vertical configuration. This experimental condition was selected to minimize ohmic heating, suppress natural convection and provided a relatively long induction time before the interfacial concentration at the cathode fell to zero. The theoretical concentration distribution (the Sand Equation) is [71],

$$C = C_b - \frac{i\eta(1-t^+)}{nFD} \cdot \left\{ 2 \left( \frac{Dt}{\pi} \right)^{1/2} \exp \left( -\frac{z^2}{4Dt} \right) - z \cdot \operatorname{erfc} \left[ \frac{z}{2(Dt)^{1/2}} \right] \right\} \quad (3.1)$$

where the term  $\eta(1-t^+)$  was added to account for migration and the current efficiency. The diffusivity  $D$  and the cation transfer number  $t^+$  are assumed constant at the bulk



concentration values given by Miller et al. [72]

Experimental values of concentration are compared with the theoretical values from Equation 3.1 as shown in Figure 3.4. Good agreement with the theoretical values is obtained if the current efficiency is taken to be 75%. This low current efficiency is probably due to the large departure from equilibrium and is likely to be a general phenomena in aggregate growth from binary solution.

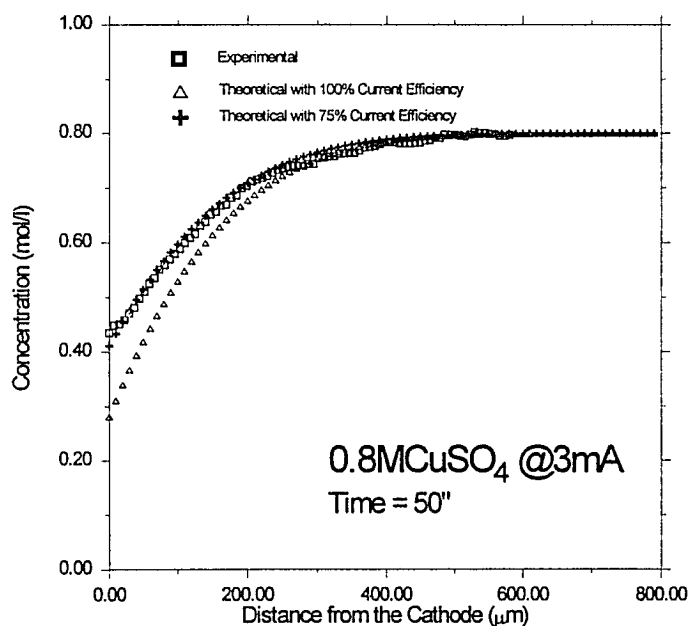


Figure 3.4: Concentration profile at 50 seconds for galvanostatic deposition from 0.8M  $CuSO_4$  in vertical cell. current density:  $40\text{ mA/cm}^2$ . The theoretical curves were computed with Equation 3.11 for current efficiencies of 100% and 75%.

## Chapter 4

# Results and Discussion

### 4.1 Morphologies

#### 4.1.1 Copper Aggregates

Morphologies of copper aggregates from  $CuSO_4$  deposition in circular cells are shown in Figure 4.1. Two typical morphologies are observed for copper deposition: tip-splitting patterns at low concentration and low applied cell potential, and the dense branch morphology (DBM) at higher concentration and higher applied cell potential.

Channel growth of copper, a morphology which is neither tip-splitting nor DBM, is observed from the deposition from 0.2M  $CuSO_4$  at 20V (Figure 4.1 (c)) in circular cells. This morphology was also reported by Garik and coworkers who called it the cellular morphology [70]. Similar patterns are also observed from the deposition from  $CuSO_4$  at parallel cells under certain experimental conditions. Figure 4.2 shows a typical channel growth of copper deposition in parallel cells.

Dendritic growth of copper deposition has not been observed in the quasi two-dimensional cells. Copper dendrites were produced in a three-dimensional cell experiment with supporting electrolyte at low cell current (Figure 4.3). This phenomenon is probably due to weak anisotropy of copper crystal in the interfacial dynamics of copper deposition from sulfate solution.



(a) 0.05M  $CuSO_4$  at 5V, 10V, 20V and 30V (from left to right).



(b) 0.1M  $CuSO_4$  at 5V, 10V, 20V and 30V (from left to right).



(c) 0.2M  $CuSO_4$  at 5V, 10V, 20V and 30V (from left to right).



(d) 0.4M  $CuSO_4$  at 5V, 10V, 20V and 30V (from left to right).

Figure 4.1: Morphology from  $CuSO_4$  deposition in horizontal circular cells. anode diameter: 25 mm, cathode diameter: 1.0 mm and cell thickness: 250  $\mu m$ .

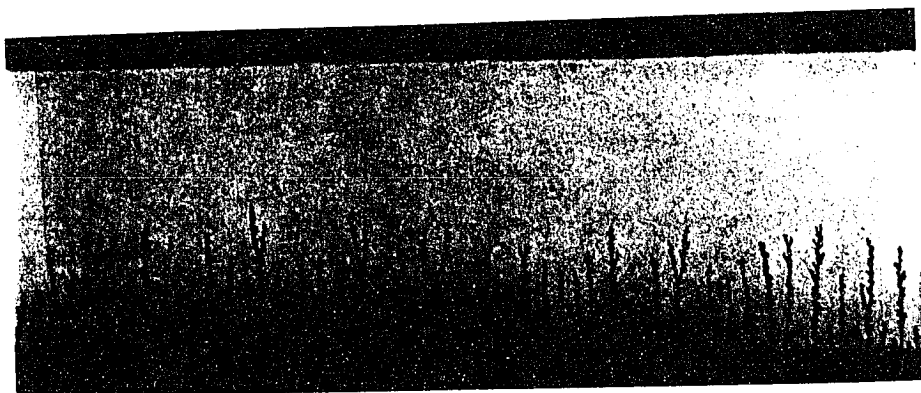


Figure 4.2: Channel growth of copper from 0.1M  $CuSO_4$  at 30 V in a parallel cell. distance between two electrodes: 10 mm, cell thickness: 100  $\mu m$ .

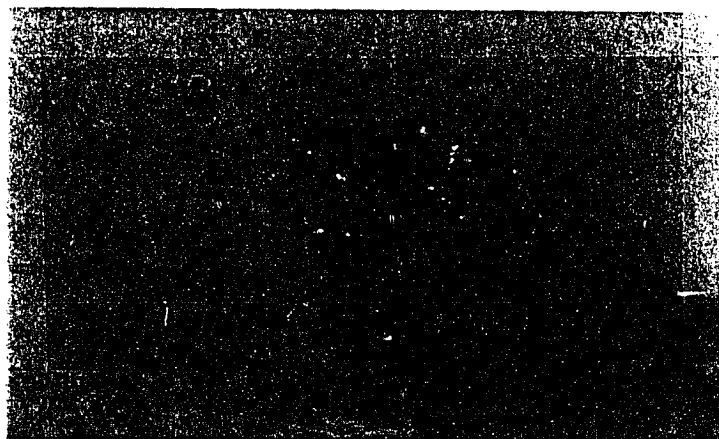


Figure 4.3: Dendritic growth of copper from 1M  $CuCl_2$  with supporting  $HCl$  at 1.4 V in a three-dimensional cell. distance between two electrodes: 10 mm.

Concentration	Cell Potential <i>V</i>	Cell Current <i>mA</i>	Growth Velocity $\mu\text{m/s}$	Morphology
0.05M	5	5	25	tip-splitting
0.05M	10	11	55	channel
0.05M	20	17.5	163	channel
0.05M	30	30	289	channel
0.1M	5	6.6	37	tip-splitting
0.1M	10	13.5	43	channel
0.1M	20	45	166	channel
0.1M	30	80	278	channel
0.2M	5	11	12	DBM
0.2M	10	31		DBM
0.2M	20	80	98.2	DBM
0.2M	30	130	165	DBM
0.4M	5	14	15	DBM
0.4M	10	36	36	DBM
0.4M	20	127	95	DBM
0.4M	30	240	120	DBM

Table 4.1: Summary of the experimental results for  $\text{CuSO}_4$  deposition. anode diameter: 25 mm, cathode diameter: 1.0 mm, and cell thickness: 250  $\mu\text{m}$ .

### 4.1.2 Zinc Aggregates

As shown in Figure 4.4, tip-splitting patterns of zinc are observed in deposition from 0.05M  $ZnSO_4$  at 5V to 30V, and dendritic growth is dominant for all applied cell potential at the concentration of 0.1M and higher in circular cells. The number of dendrites in a cell increases with higher applied potential or lower electrolyte concentration. The tip radii have similar dependence on applied potential and concentration.

Pattern selection of zinc deposition from  $ZnSO_4$  in parallel cells is generally consistent with the phase diagram of Sagues et. al. [42] (Figure 2.4 (b)). The cell thickness in their case is thinner (75  $\mu m$ ) so the location of the patterns transition boundary is slightly different from our experimental observation.

In the horizontal cell configuration, dendrites are produced with  $ZnSO_4$  solution for the concentration between 0.04M to 0.3M at appropriate cell potentials as shown in Figure 4.5 (a) and 4.18 (a). The dependence of applied potential and concentration on the number of dendrites and their tip radii is the same as in circular cells.

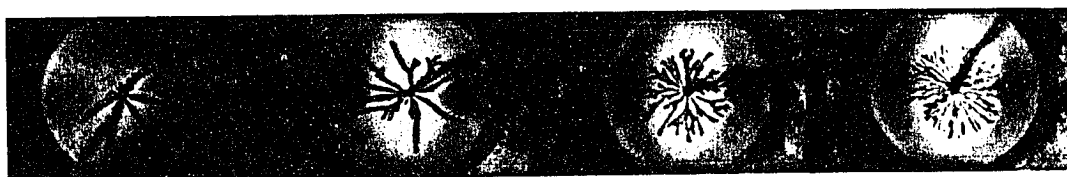
Channel growth is observed in deposition from 0.02M  $ZnSO_4$  in the horizontal cell (Figure 4.6). The branches produced in zinc channel growth are neither tip-splitting nor dendritic, but progress in the same direction with the same growth velocity and retaining the same gap spacing in between. Channel growth in zinc deposition was first reported by Trigueros and coworkers, in which they observe the shift from channel growth to dendrites at about 0.06M in their thinner cell [41]. In our experiments, channel growth can be produced in deposition from  $ZnSO_4$  at concentrations from 0.02M to 0.3M in vertical cells at appropriate applied potentials (Figure 4.5 (b) and 4.18 (b)). The experimental results for deposition from  $ZnSO_4$  in circular cells and for deposition from  $CuSO_4$  and  $ZnSO_4$  in parallel cells are summarized in Table 4.2 and Table 4.3, respectively.



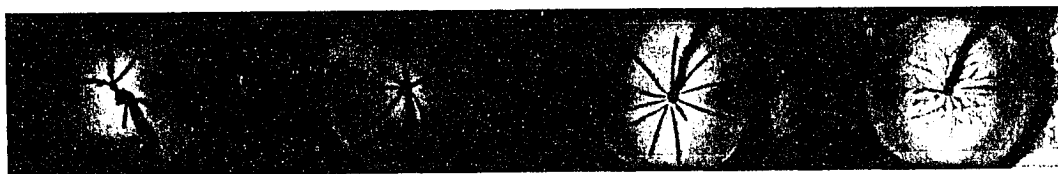
(a) 0.05M  $ZnSO_4$  at 5V, 10V, 20V and 30V (from left to right).



(b) 0.1M  $ZnSO_4$  at 5V, 10V, 20V and 30V (from left to right).



(c) 0.2M  $ZnSO_4$  at 5V, 10V, 20V and 30V (from left to right).



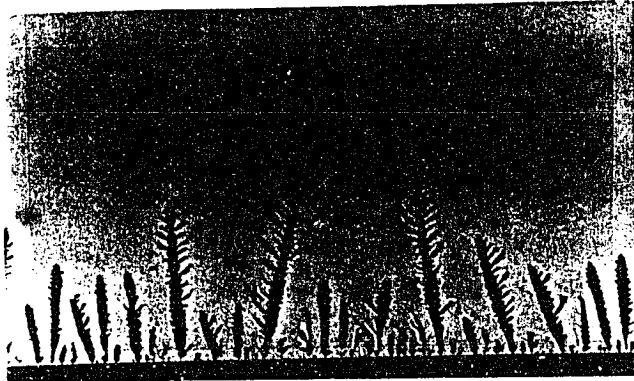
(d) 0.4M  $ZnSO_4$  at 5V, 10V, 20V and 30V (from left to right).

Figure 4.4: Morphology from  $ZnSO_4$  deposition in horizontal circular cells. anode diameter: 25 mm, cathode diameter: 1.0 mm and cell thickness: 250  $\mu m$ .

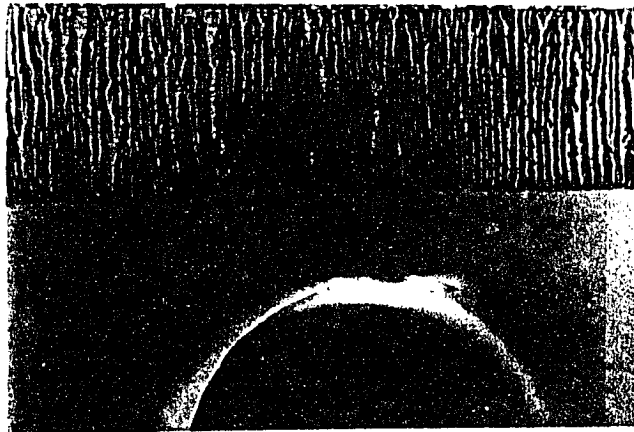
Concentration	Cell Potential <i>V</i>	Cell Current <i>mA</i>	Growth Velocity $\mu\text{m}/\text{s}$	Morphology
0.05M	5	4		tip-splitting
0.05M	10	11		tip-splitting
0.05M	20	40		tip-splitting
0.05M	30	42		tip-splitting
0.1M	5	5.7		dendrite
0.1M	10	16		dendrite
0.1M	20	38		dendrite
0.1M	30	74		dendrite
0.2M	5	9.2	22	dendrite
0.2M	10	19	90	dendrite
0.2M	20	61	161	dendrite
0.2M	30	102	374	dendrite
0.4M	5	15	47	dendrite
0.4M	10	38	137	dendrite
0.4M	20	85		dendrite
0.4M	30	260	515	dendrite

Table 4.2: Summary of the experimental results for deposition from  $ZnSO_4$  in horizontal circular cells. anode diameter: 25 mm, cathode diameter : 1.0 mm and cell thickness: 250  $\mu\text{m}$ .





(a) dendrite in horizontal cell.



(b) channel growth in vertical cell.

Figure 4.5: Morphology produced by deposition from 0.04M  $ZnSO_4$  at 30 V in horizontal and vertical parallel cells. cell thickness:  $100\mu m$ , distance between two electrodes:  $30mm$

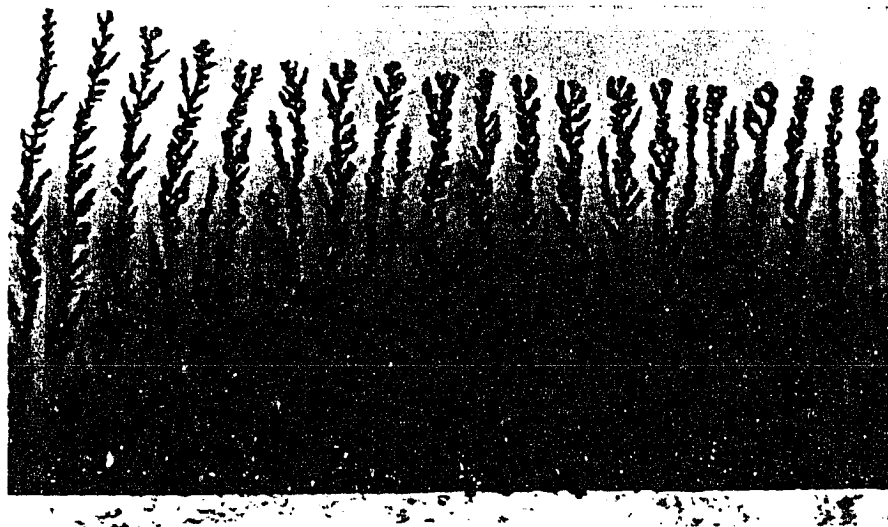


Figure 4.6: Channel growth from deposition from 0.02M  $ZnSO_4$  at 35 V in horizontal parallel cell. cell thickness:  $100\mu m$ , distance between two electrodes: 30mm

## 4.2 Concentration Profiles

Gray-scale interferometric images and the concentration profiles computed from the images for aggregate growth from ECD will be presented in this section. The darkness in an image represents the magnitude of the concentration at that point. Contours of the same gray level are iso-concentration curves in the image. Quantitative concentration profiles are computed from the corresponding images as discussed in Appendix A.

### 4.2.1 Copper Deposition

Gray-scale image for tip-splitting morphology produced by deposition from 0.05M  $CuSO_4$  at 25 V is given in Figure 4.7 (a). The concentration distribution near a growing tip of the aggregates is computed from the image and given in Figure 4.7 (b).

The dense-branched morphology or DBM is produced by deposition from 0.2M and 0.4M  $CuSO_4$  in horizontal circular or parallel at 15 V and 30 V cells, respectively. The gray-scale images are given in Figure 4.8 and Figure 4.9. Gray-scale display of the concentration around aggregates in each case forms a smooth envelope in front of the aggregates.

Solution	Cell Potential $V$	Configuration			Cell Current $mA$	Velocity $\mu m/s$	Morphology
		$t$	$d$	Orien.			
0.1M $CuSO_4$	20	250	10	hor.		177.2	channel
0.1M $CuSO_4$	20	100	10	ver.	20	69.8	channel
0.1M $CuSO_4$	20	100	10	hor.		101.3	channel
0.1M $CuSO_4$	13	100	10	hor.		83.0	channel
0.1M $CuSO_4$	13	100	10	ver.		77.2	channel
0.2M $CuSO_4$	15	250	20	hor.	26.7	18	DBM
0.2M $CuSO_4$	30	250	20	hor.	61.4	40	DBM
0.4M $CuSO_4$	15	250	20	hor.	43.8	18	DBM
0.4M $CuSO_4$	30	250	20	hor.	50.4	33	DBM
0.4M $CuSO_4$	15	250	20	ver.	25.9	19	tip-split
0.3M $ZnSO_4$	8	100	10	hor.		24.3	dendrites
0.3M $ZnSO_4$	8	100	10	ver.		15.8	channel
0.1M $ZnSO_4$	42	100	10	ver.		114.2	channel
0.02M $ZnSO_4$	35	100	30	hor.	4.5	$\approx 2.5$	channel
0.3M $ZnSO_4$	25	100	30	hor.	5.0	$\approx 1.0$	dendrites

Table 4.3: Summary of experimental results for electrodeposition in parallel cells.  $t$  stands for cell thickness in  $\mu m$ ,  $d$  is the distance between two electrodes in  $mm$ , hor. = horizontal cell; ver. = vertical cell.

The concentration profiles along the direction of growth are given in Figure 4.10. The concentration gradients are independent of the applied potential and cell configuration (circular or parallel). This phenomenon is probably due to the influence of natural convection effects on the concentration distribution in the boundary layer near the aggregates.

Channel growth of copper aggregates is formed by deposition from 0.1M  $CuSO_4$  in circular and parallel cells. The orientation of a parallel cell in the vertical or horizontal direction has a negligible effect on morphology selection within the range of copper channel growth in our experiment. Gray-scale images for copper channel growth are given in Figure 4.11, 4.12 and 4.13. The concentration profiles in between the branches along the growth direction are given in Figure 4.14 and 4.15. The concentration profile in between two branches normal to the growth direction is shown in Figure 4.16. The bulk solution penetrates into the spaces in between the branches and the smooth concentration boundary is formed around each branch.

### 4.2.2 Zinc Deposition

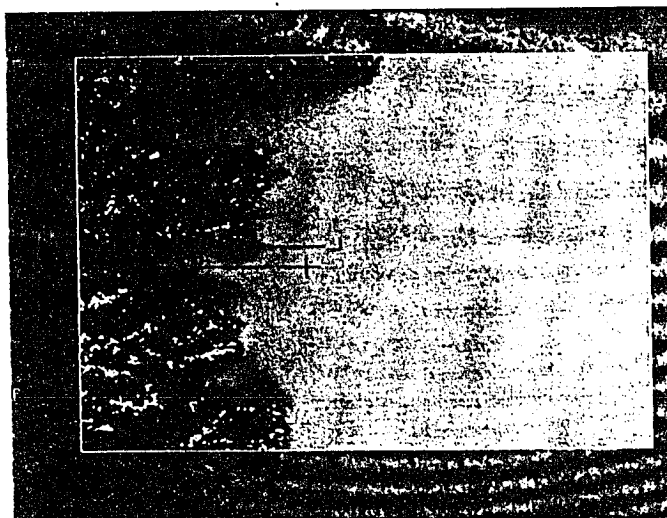
Gray-scale images for zinc dendrites produced by deposition from 0.2M and 0.3M  $ZnSO_4$  in circular and parallel cells in horizontal configuration are shown in Figure 4.17 (a) and 4.18 (a), respectively. The concentration boundary layer is thinner at the growing tips than that at the dendritic surface farther away from the tips. The concentration profiles from the image are given in Figure 4.17 (b). The concentration gradient at the tip is much steeper than those farther away from the tip.

A gray-scale image and the corresponding concentration profile for zinc channel growth in deposition from 0.02M  $ZnSO_4$  in horizontal cell is given in Figure 4.19. The arc shape concentration distribution at the branch tips can be observed from the image. The bulk solution does not penetrate into the gap in between branches.

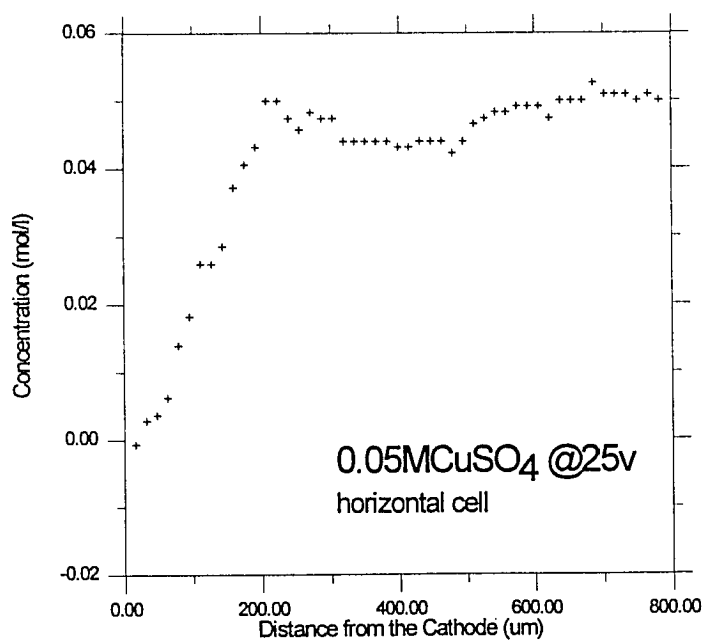
Dendrites are formed by deposition from 0.04  $ZnSO_4$  and 0.3M  $ZnSO_4$  in horizontal cells, while channel growth is obtained in deposition from the same concentration at the same applied potential in vertical cells. Figure 4.18 and 4.20 show the gray-scale images. The concentration profiles from the images are given in Figure 4.21 and 4.22. The concentration gradients are steeper for channel growth in vertical cells than those for dendrites in horizontal cells.

Though channel growth of zinc in deposition from  $ZnSO_4$  from the concentration higher than 0.06M has not been produced even at an extremely high applied potential (108 V), zinc channels can be obtained at concentrations of higher than 0.06M at moderate applied potentials in vertical cells.

The gray-scale image and concentration profile for channel growth in deposition from 0.1M  $ZnSO_4$  at 42 V in vertical cell is given in Figure 4.23. The concentration in between the branches is depleted to zero.



(a) Gray-scale image. image frame:  $5990\mu m \times 3872\mu m$ .

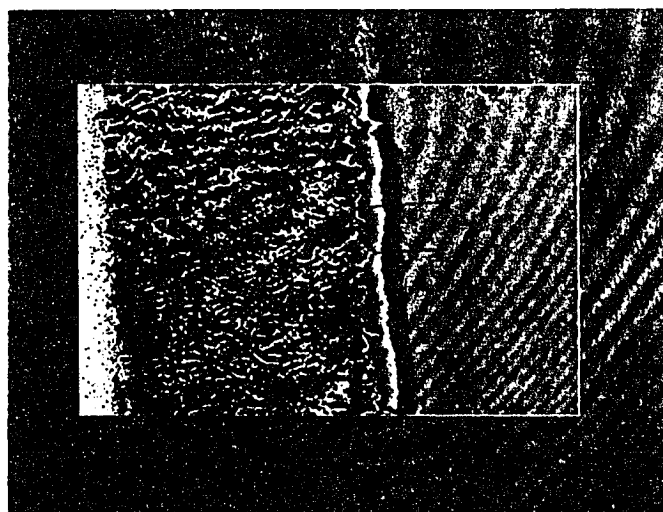


(b) Concentration profile along the direction of growth.

Figure 4.7: Gray-scale image and concentration profile during deposition from  $0.05M CuSO_4$  at  $25 V$  in horizontal parallel cell. cell thickness:  $250 \mu m$ , distance between two electrodes:  $30 mm$ .

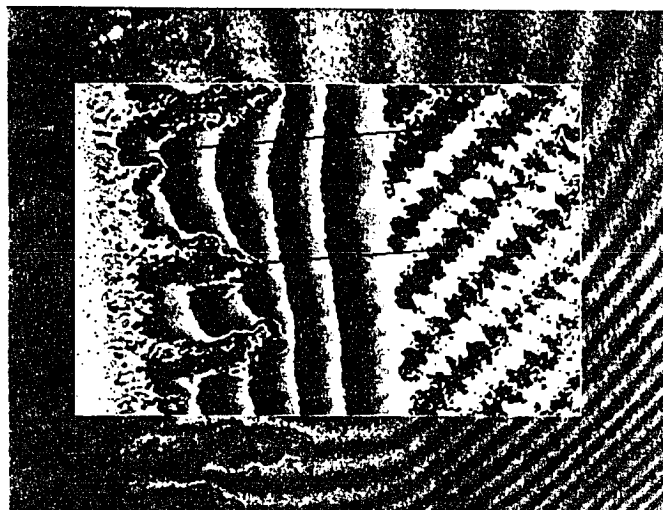


(a) cell applied potential: 15 V.

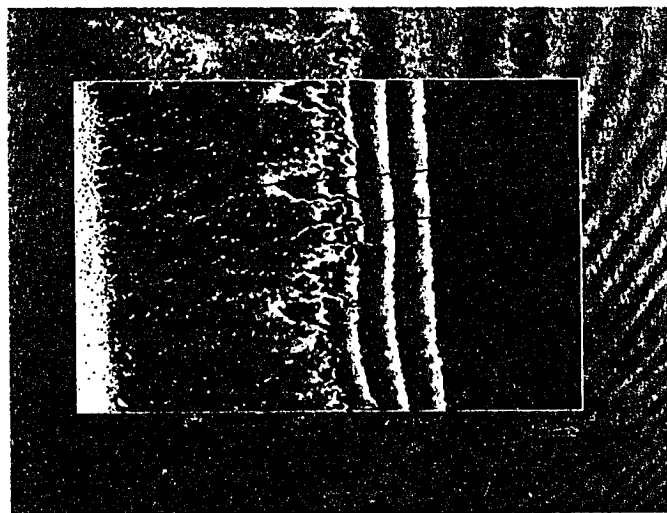


(b) cell applied potential: 30 V.

Figure 4.8: Gray-scale images during deposition from 0.2M  $CuSO_4$  at 15 V and 30 V in horizontal parallel cell. cell thickness: 250  $\mu m$ , distance between two electrodes: 20 mm, image frame: 5990 $\mu m$   $\times$  3872 $\mu m$ .



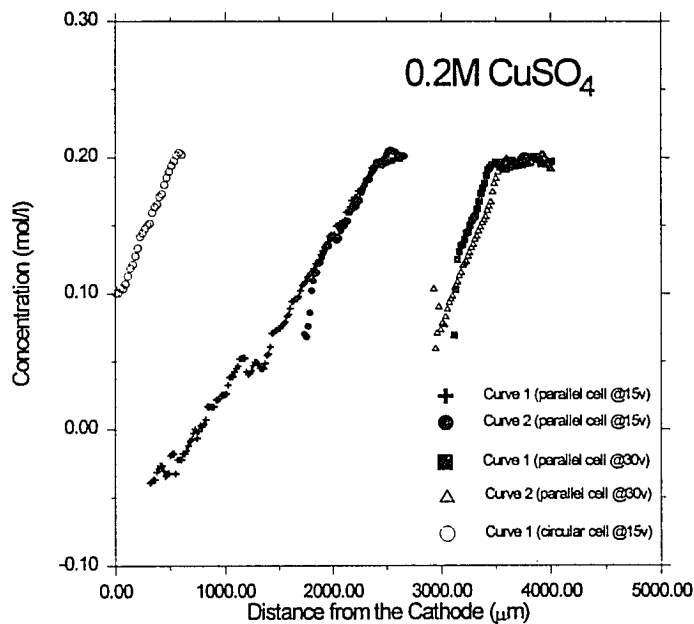
(a) cell applied potential: 15 V.



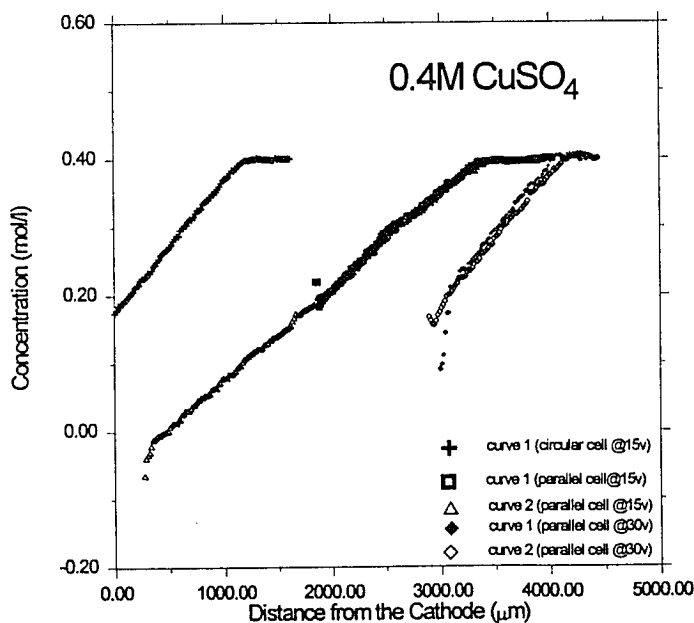
(b) cell applied potential: 30 V.

Figure 4.9: Gray-scale images during deposition from 0.4M  $CuSO_4$  at 15 V and 30 V in horizontal parallel cell. cell thickness: 250  $\mu m$ , distance between two electrodes: 20 mm, image frame: 5990 $\mu m \times$  3872 $\mu m$ .





(a) Concentration profile along the direction of growth for 0.2M  $\text{CuSO}_4$ .

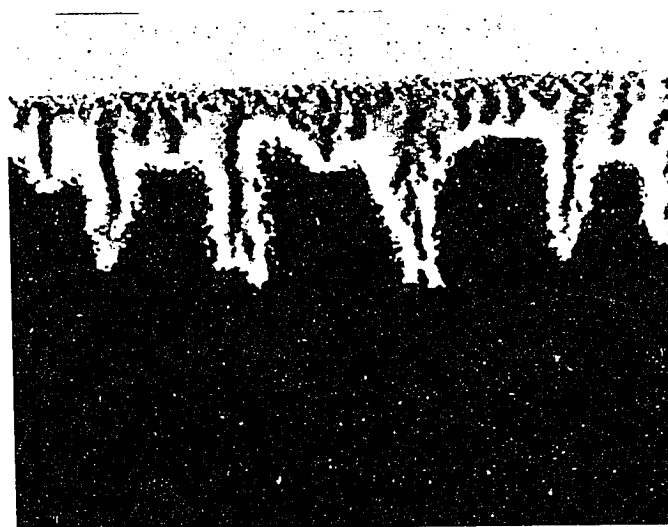


(b) Concentration profile along the direction of growth for 0.4M  $\text{CuSO}_4$ .

Figure 4.10: Concentration profiles during deposition from  $\text{CuSO}_4$  in horizontal circular and parallel cells. circular cell: anode diameter = 25 mm, cathode diameter = 1.0 mm, cell thickness = 250  $\mu\text{m}$ . parallel cell: distance between two electrodes = 20 mm, cell thickness = 250  $\mu\text{m}$ .



(a) channel growth in horizontal configuration, image frame:  $7747\mu\text{m} \times 6087\mu\text{m}$ .



(b) channel growth downward in vertical configuration, image frame:  $4478\mu\text{m} \times 3662\mu\text{m}$ .

Figure 4.11: Gray-scale images during deposition from  $0.1\text{M } \text{CuSO}_4$  at  $20\text{ V}$  in horizontal and vertical parallel cell. cell thickness:  $100\ \mu\text{m}$ , distance between two electrodes:  $10\ \text{mm}$ .



(a) channel growth in horizontal configuration, image frame:  $7747\mu m \times 6087\mu m$ .



(b) channel growth downward in vertical configuration, image frame:  $4478\mu m \times 3662\mu m$ .

Figure 4.12: Gray-scale images during deposition from  $0.1M CuSO_4$  at  $13 V$  in horizontal and vertical parallel cell. cell thickness:  $100 \mu m$ , distance between two electrodes:  $10 mm$ .

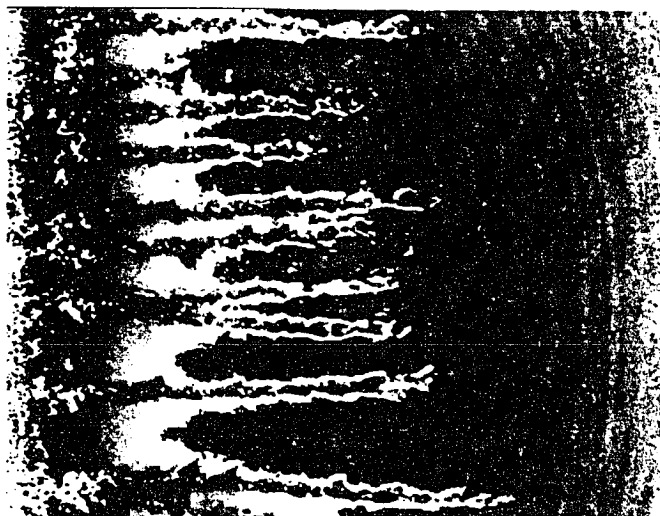


Figure 4.13: Gray-scale images during deposition from 0.1M  $CuSO_4$  at 20 V in horizontal parallel cell. cell thickness: 250  $\mu m$ , distance between two electrodes: 10 mm, image frame: 7747 $\mu m \times$  6087 $\mu m$ .

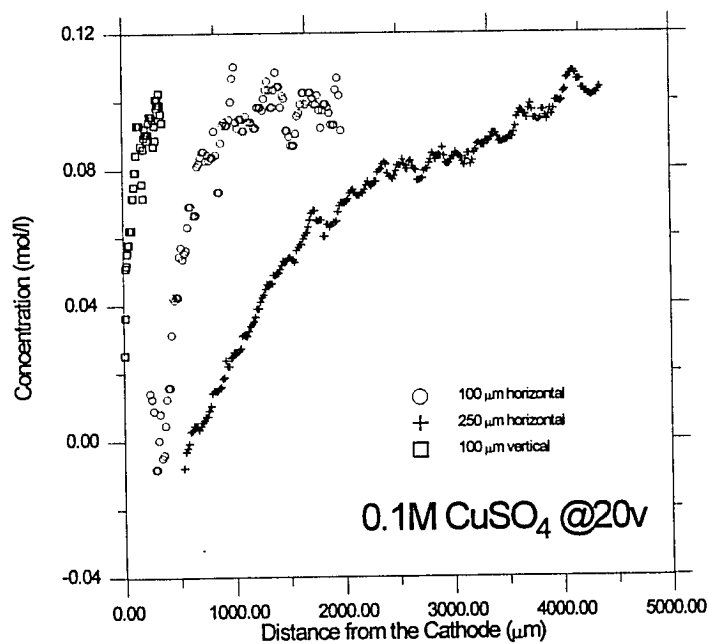


Figure 4.14: Concentration profiles during deposition from 0.1M  $CuSO_4$  at 20 V in horizontal and vertical parallel cells. distance between two electrodes = 10 mm, cell thickness = 100 or 250  $\mu m$ .

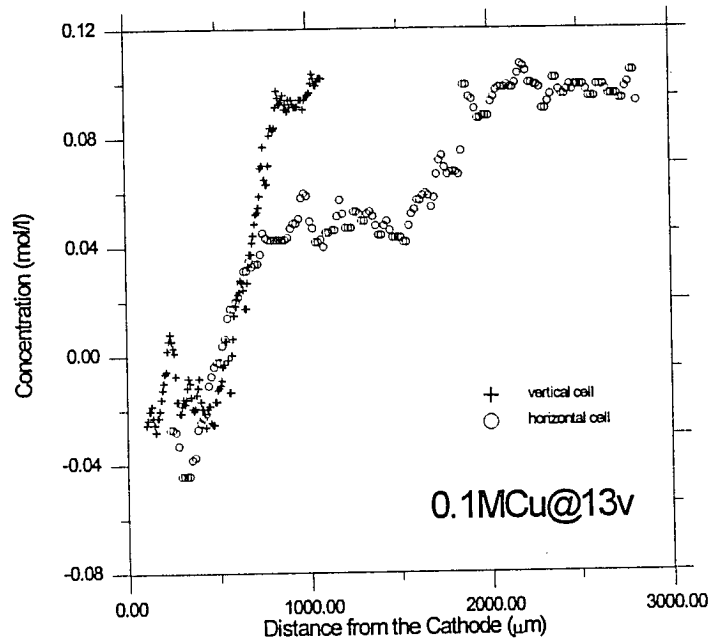


Figure 4.15: Concentration profiles during deposition from  $0.1M CuSO_4$  at  $13 V$  in horizontal and vertical parallel cells. distance between two electrodes =  $10 mm$ , cell thickness =  $100 \mu m$ .

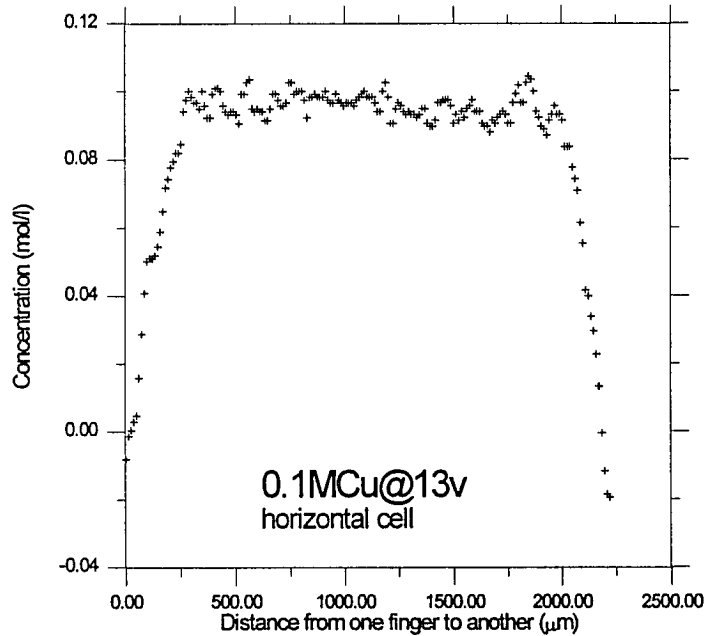


Figure 4.16: Concentration profile normal to the growth direction in between two branches during deposition from  $0.1M CuSO_4$  at  $13 V$  in horizontal parallel cells. cell thickness:  $100 \mu m$ , distance between two electrodes:  $10 mm$ .

## 4.3 Convection Effects

### 4.3.1 Theoretical Model

The full convection problem in electrochemical deposition is governed by natural convection due to concentration and temperature gradients as well as electrokinetic effects. Let us first assume that the electrodeposition process is controlled by diffusion only. For a binary solution, with the assumption of electroneutrality, the electrostatic and concentration fields can be decoupled and treated separately [69]. For steady state aggregate growth without convection in a one dimensional cell, the concentration profile in the normal direction obeys the diffusion equation

$$\frac{d^2C}{dx^2} + \frac{v}{D} \frac{dC}{dx} = 0 \quad (4.1)$$

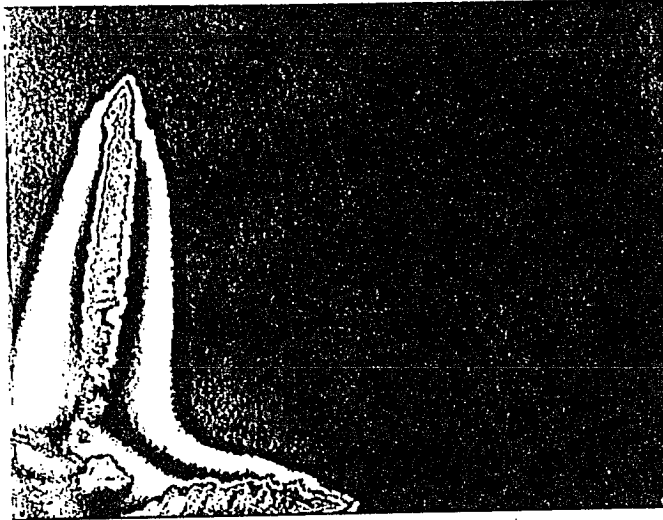
where  $v$  is the steady state growth velocity,  $D$  the diffusivity and  $x$  the distance from the growth front. A solution of equation 4.1 is obtained as

$$C = C_b - (C_b - C_i) \exp\left(-\frac{v}{D}x\right) \quad (4.2)$$

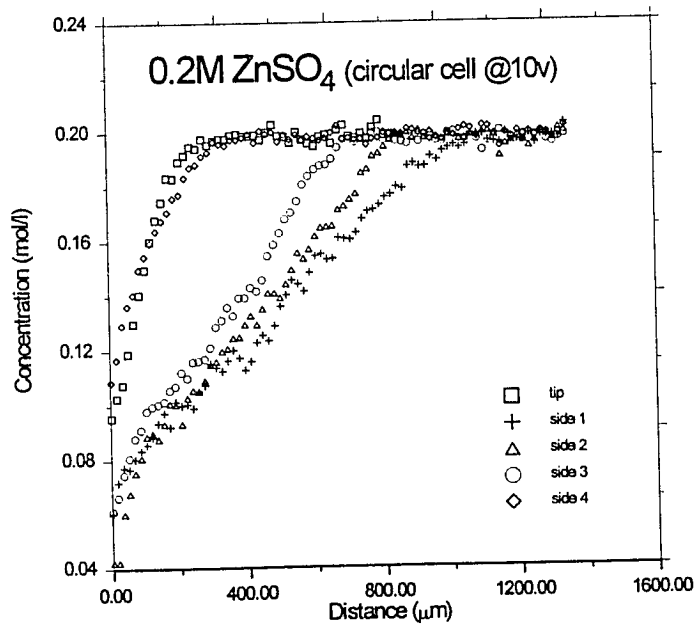
where  $C_b$  and  $C_i$  are the bulk and interfacial concentration, respectively.

The concentration is  $C_i$  at the interface and approaches 96% of the bulk value with a length constant  $3D/v$  which can be compared with measured values. For copper DBM deposition in the horizontal configuration, the measured width of the concentration boundary layer is an order of magnitude greater than the length constant given in the diffusion model, and the discrepancy increases with increasing concentration. This effect must be the result of natural convection.

The dominant parameter in natural convection problems is the Grashof number, which is defined as



(a) gray-scale image. image frame:  $5990\mu\text{m} \times 3872\mu\text{m}$ .

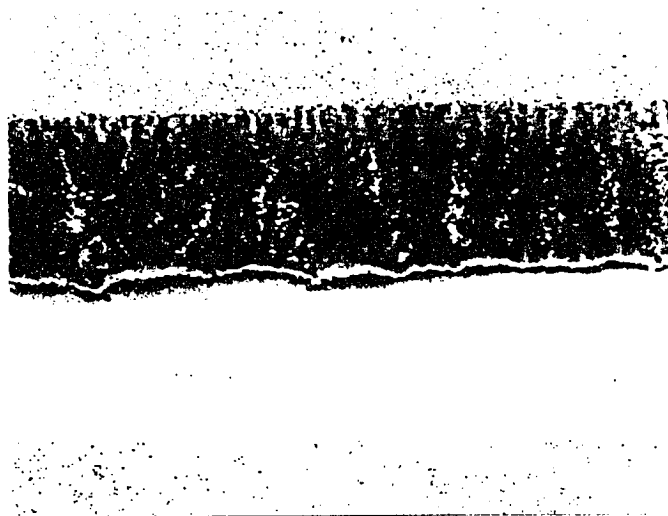


(b) concentration profiles around a dendrite normal to the interface.

Figure 4.17: Gray-scale image and concentration profile during deposition from  $0.2\text{M ZnSO}_4$  at  $25\text{ V}$  in horizontal circular cell. anode diameter =  $25\text{ mm}$ , cathode diameter =  $1.0\text{ mm}$ , cell thickness =  $250\ \mu\text{m}$ .



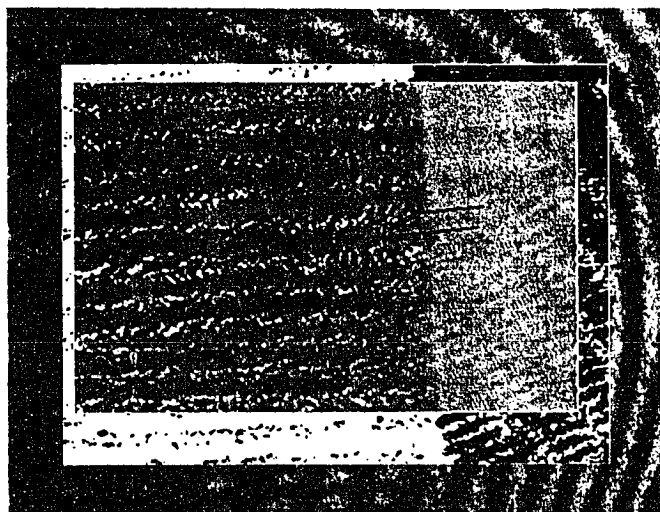
(a) dendrites formed in horizontal configuration, image frame:  $7747\mu m \times 6087\mu m$ .



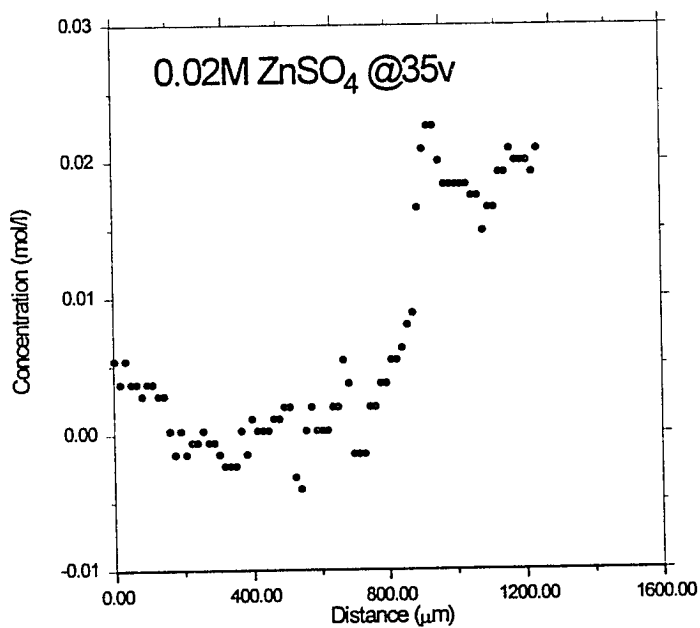
(b) channel growth produce in downward vertical configuration, image frame:  
 $4478\mu m \times 3662\mu m$ .

Figure 4.18: Gray-scale images during deposition from  $0.3M ZnSO_4$  at  $8 V$  in horizontal and vertical parallel cell. cell thickness:  $100 \mu m$ , distance between two electrodes:  $10 mm$ .





(a) Gray-scale image. image frame:  $5990\mu\text{m} \times 3872\mu\text{m}$ .



(b) Concentration profile along the direction of growth.

Figure 4.19: Gray-scale image and concentration profile during deposition from  $0.02\text{M ZnSO}_4$  at  $35\text{ V}$  in horizontal parallel cell. cell thickness:  $100\ \mu\text{m}$ , distance between two electrodes:  $30\ \text{mm}$ .



(a) dendrites grow in horizontal configuration, image frame:  $5990\mu m \times 3872\mu m$ .



(b) channel growth produce in downward vertical configuration, image frame:  
 $2486\mu m \times 1964\mu m$ .

Figure 4.20: Gray-scale images during deposition from  $0.04M ZnSO_4$  at  $30 V$  in horizontal and vertical parallel cells. cell thickness:  $100 \mu m$ , distance between two electrodes:  $30 mm$ .

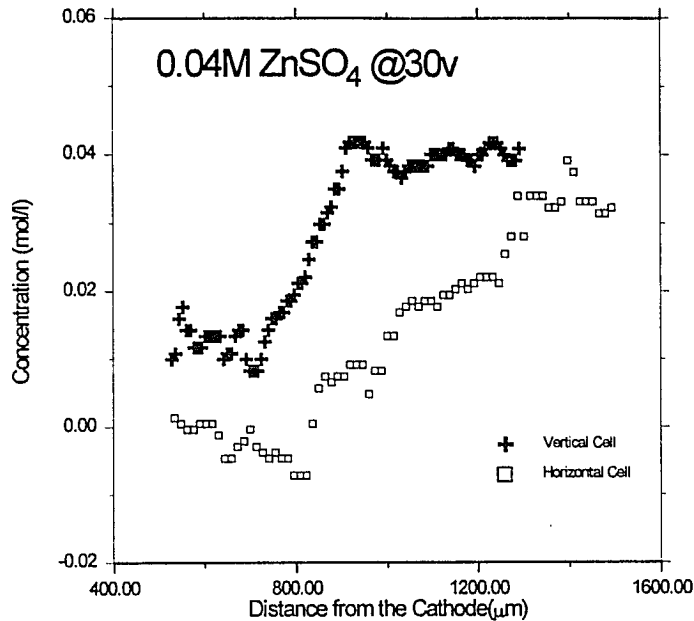


Figure 4.21: Concentration profiles during deposition from 0.04M  $ZnSO_4$  at 30 V in horizontal and vertical parallel cell. distance between two electrodes = 30 mm, cell thickness = 100  $\mu m$ .

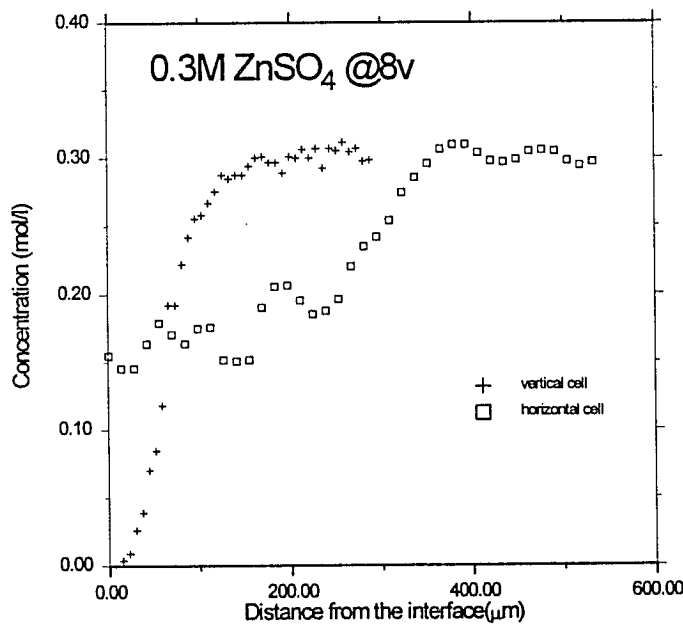
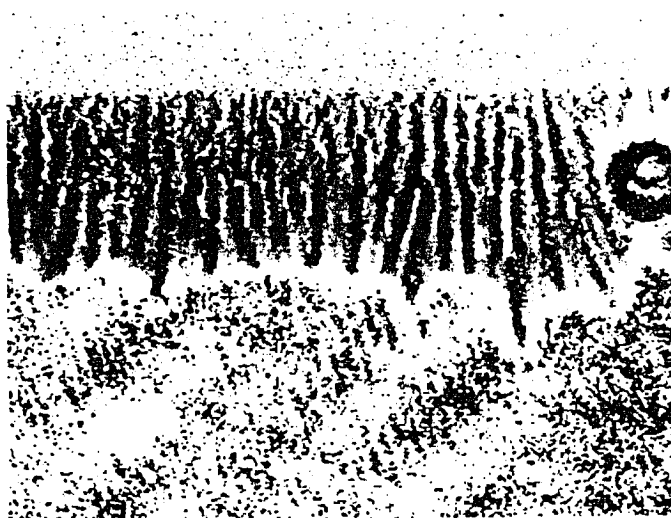
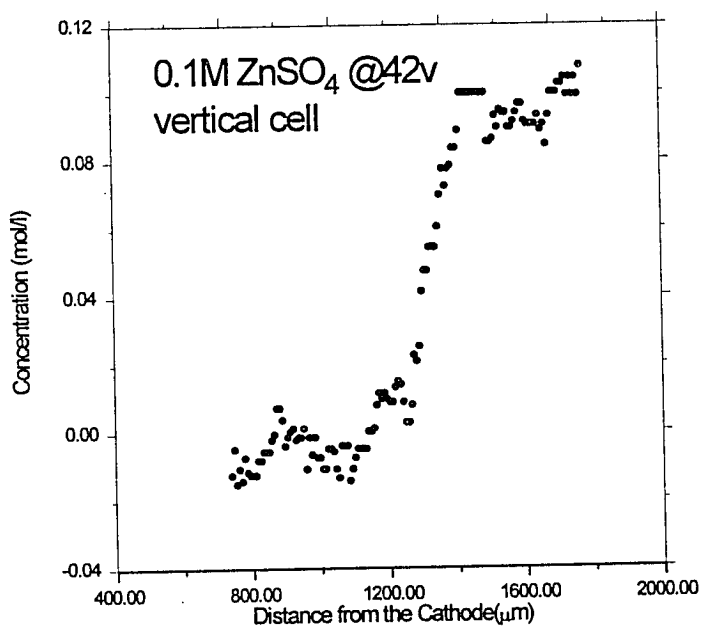


Figure 4.22: Concentration profiles during deposition from 0.3M  $ZnSO_4$  at 8 V in horizontal and vertical parallel cell. distance between two electrodes = 10 mm, cell thickness = 100  $\mu m$ .



(a) Gray-scale image. image frame:  $4478\mu\text{m} \times 3662\mu\text{m}$ .



(b) Concentration profile along the direction of growth.

Figure 4.23: Gray-scale image and concentration profile during deposition from  $0.1\text{M ZnSO}_4$  at  $42\text{ V}$  in vertical parallel cell. cell thickness:  $100\ \mu\text{m}$ , distance between two electrodes:  $10\ \text{mm}$ .

$$Gr = \frac{g\Delta\rho L^3}{\nu^2\rho_o} \quad (4.3)$$

where  $g$  is the gravitational acceleration,  $\Delta\rho$  the density difference due to a concentration or temperature difference,  $L$  the thickness of the cell,  $\nu$  the kinematic viscosity of the solution and  $\rho_o$  the density in the bulk. Natural convection increases with increasing Grashof number.

As shown in Figure 4.24, we applied the Navier-Stokes equation to the boundary layer in the horizontal configuration. The continuity equation is

$$\frac{\partial u}{\partial x} + \frac{\partial v}{\partial y} = 0 \quad (4.4)$$

where  $v$  and  $u$  are the velocity component in vertical and horizontal direction, respectively. This equation can be simplified as

$$\frac{v}{H} \sim \frac{u}{\delta}$$

where  $H$  is the thickness of a cell and  $\delta$  is the thickness of the boundary layer. Therefore, the horizontal velocity component  $u$  is given

$$u \sim \frac{v \cdot \delta}{H} \quad (4.5)$$

The Navier-Stokes equation for this boundary layer in the vertical direction gives

$$u \frac{\partial v}{\partial x} + v \frac{\partial v}{\partial y} = \frac{g\Delta\rho}{\rho_o} + \nu \frac{\partial^2 v}{\partial x^2} \quad (4.6)$$

where  $\nu$  is the kinematic viscosity,  $\Delta\rho$  the density difference due to concentration depletion in the boundary layer, and  $\rho_o$  the density of bulk solution.

The mass balance gives the corresponding concentration equation in the boundary layer

as

$$u \frac{\partial C}{\partial x} + v \frac{\partial C}{\partial y} = D \frac{\partial^2 C}{\partial x^2} \quad (4.7)$$

where  $D$  is the diffusivity and  $C$  is the concentration.

Equation 4.7 can be approximated in the boundary layer as

$$u \frac{\Delta C}{\delta} + v \frac{\Delta C}{H} \sim D \frac{\Delta C}{\delta^2} \quad (4.8)$$

Combining this equation with Equation 4.5, we have

$$v \sim D \frac{H}{\delta^2} \quad (4.9)$$

Equation 4.6 can be approximated by

$$\frac{v^2}{H} \sim \frac{g \Delta \rho}{\rho_o} + \nu \frac{v}{\delta^2} \quad (4.10)$$

Combining the above two equations, we have

$$\frac{DH}{\delta^4} + \frac{\nu H}{\delta^4} \sim \frac{g \Delta \rho}{\rho_o} \quad (4.11)$$

For  $CuSO_4$  and  $ZnSO_4$  electrolytes, the Schmidt number,  $Sc = \frac{\nu}{D}$  is in the order of 1000, the above equation can be approximated by

$$\left( \frac{H}{\delta} \right)^4 \sim \frac{g \Delta \rho H^3}{D \rho_o} \quad (4.12)$$

or it is written as

$$\left( \frac{\delta}{H} \right) \sim (Ra)^{-1/4} \quad (4.13)$$

where  $Ra$  is the Rayleigh number,  $Ra = Gr \cdot Sc$ , and  $Sc$  is the Schmidt number. Substituting  $\delta$  in the above equation back to Equation 4.9, we obtain the velocity component in the vertical direction in a horizontal cell

$$v_{\parallel} = \frac{D}{H} \cdot \sqrt{Ra} \quad (4.14)$$

In the case of deposition in a vertical cell, a force balance over a control volume in the vertical direction gives

$$\mu \frac{\partial v}{\partial x} = g \Delta \rho \cdot H/2 \quad (4.15)$$

Simplifying the above equation in the boundary layer, we obtain

$$\mu \frac{v}{H} \sim \frac{g \Delta \rho \cdot H}{2} \quad (4.16)$$

Rearranging, we get

$$v_{\perp} \sim \frac{g \Delta \rho \cdot H^2}{2\mu} = \frac{D}{2H} \cdot Ra \quad (4.17)$$

Combining the above equation with Equation 4.14, we obtain the ratio of electrolyte velocity in vertical cell to that in horizontal cell as follows

$$\frac{v_{\perp}}{v_{\parallel}} \sim \sqrt{\frac{Ra}{2}} \quad (4.18)$$

For 0.1M  $CuSO_4$  or 0.1M  $ZnSO_4$  deposition in a vertical cell or a horizontal cell with a cell thickness of  $100\mu m$ , this ratio is 0.067. The numerical results of this model indicate natural convection is much stronger in a horizontal cell than that in a vertical cell.

### 4.3.2 Experimental Observation

Natural convection is observed in our experiment when 1% rheoscopic microparticles are added to  $CuSO_4$  or  $ZnSO_4$  solution in a cell with a thickness of  $790\ \mu m$ . The movement of the solution near the cathode was observed and can be illustrated in Figure 4.24.

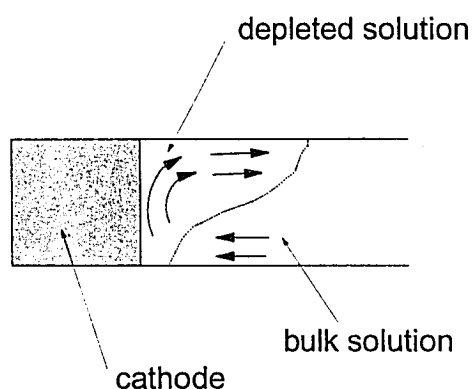


Figure 4.24: Demonstration of natural convection observed in copper or zinc deposition from  $CuSO_4$  or  $ZnSO_4$  in circular and parallel cell with the thickness of  $790\ \mu m$ .

This phenomenon can be explained as follows. The depleted solution, of lower density, rises in front of the deposit, while bulk solution is convected toward the deposit along the lower plate. A plume of the depleted solution at the top of the cell flows away from the deposit along the upper plate. In these very thin cells in our experiment, the plume occupies a considerable fraction of the cell thickness. This broadening of the boundary layer is contrary to the normal understanding that the stronger the convection, the thinner the concentration boundary layer. However, a wider concentration boundary layer caused by plume movement is observed with stronger convection in these thin cells, since the concentration measured in our experiment is only the vertically averaged concentration.

From the definition of the Grashof number, natural convection increases in strength with



increasing cell thickness  $L$ , which can be illustrated in the deposition from 0.1M  $CuSO_4$  in horizontal cells with cell thicknesses of 100  $\mu m$  and 250  $\mu m$ , respectively. As shown in Figure 4.14, the thickness of concentration boundary layer is 1000  $\mu m$  in the thin cell, while it is 4500  $\mu m$  in the thicker cell.

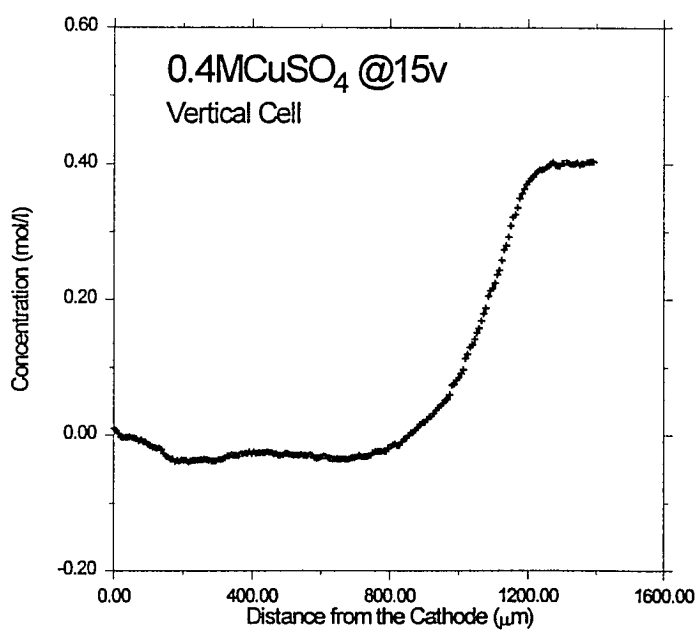
The higher the concentration, the greater is the density difference between the bulk and depleted solution and the greater is the Grashof number. Natural convection is therefore stronger in more concentrated solutions. Figure 4.10 shows the concentration profiles for deposition from 0.2M  $CuSO_4$  and 0.4M  $CuSO_4$  in horizontal cells at 15 V. The concentration boundary layer is 2400  $\mu m$  for the less concentrated solution and 3200  $\mu m$  for the more concentrated solution.

The observed morphology for deposition from 0.2M  $CuSO_4$  and 0.4M  $CuSO_4$  in horizontal cells is the DBM. In the vertical cell, the aggregates change to fingers in deposition from 0.2M  $CuSO_4$  (Figure 4.25 (a)). The concentration boundary layer in front of the fingers is too thin to resolve in our measurement. Between the fingers, the concentration gradient is much steeper than in the horizontal cells. We cannot develop a quantitative model of this complicated boundary layer, but only remark that it broadens diffusively. The penetration length given in the diffusion model is  $\sqrt{4Dt}$  (where  $D$  is the diffusivity and  $t$  the time from the beginning of electrodeposition). This value is 380  $\mu m$  at the time of measurement in Figure 4.25 (b), which is close to the observed width. The transition from the depleted electrolyte to the bulk takes place between roughly 800 and 1200  $\mu m$  from the cathode.

We conclude that natural convection is suppressed in the vertical configuration but is significant in the horizontal configuration, where the depleted solution lies on top of the bulk solution.



(a) Gray-scale image. image frame:  $5990\mu\text{m} \times 3872\mu\text{m}$ .

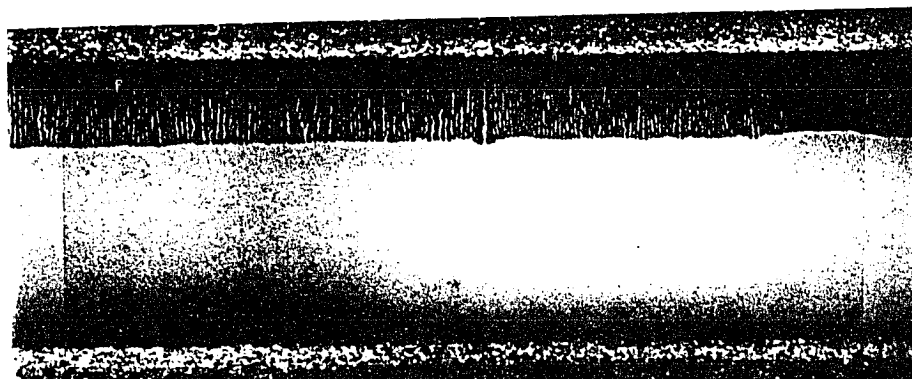


(b) Concentration profile along the direction of growth.

Figure 4.25: Gray-scale image and concentration profile during deposition from  $0.2\text{M } \text{CuSO}_4$  at  $15\text{ V}$  in vertical parallel cell. cell thickness:  $100\ \mu\text{m}$ , distance between two electrodes:  $30\ \text{mm}$ .

#### 4.4 Comparison of Zinc and Copper Channel Growth

Typical channel growth of zinc and copper in parallel cells is shown in Figure 4.26. The characteristics of zinc and copper channels and the conditions under which they are formed are listed in Table 4.4.



(a) 0.06M  $ZnSO_4$  at 45V



(b) 0.1M  $CuSO_4$  at 20V

Figure 4.26: Channel growth in deposition from  $ZnSO_4$  and  $CuSO_4$  in horizontal parallel cells. cell thickness:  $100\mu m$ , distance between two electrodes:  $10mm$

The concentration range of  $CuSO_4$  over which channel patterns can be formed is quite different from that of  $ZnSO_4$ . Copper channels can exist at higher concentration and a wider concentration range in horizontal cells. Zinc channels are much denser. However, both copper and zinc channel growth can only be produced at relatively strong electric field

Conditions/Characteristics	Zinc channel	Copper channel
Concentration	0.02M – 0.06M	0.05M – 0.2M
Cell potential	10V – 50V	20V – 60V
Distance between channels	0.17mm – 0.5mm	≈ 1.0mm
Concentration between channels	≈ 0	≫ 0

Table 4.4: Channel Growth of  $ZnSO_4$  and  $CuSO_4$  Deposition in horizontal parallel cells.

(high cell potential). The gravity force has significant effects on the morphology of zinc deposition, while no such effect has been found on copper deposition. Further investigation into this problem is presented in section 4.5.

Garik and coworkers [70] argued that the stability and regular spacing of the branches in their cellular morphology were due to cellular convection induced by gradient stresses. Under this hypothesis, the spacing of branches is determined by the scale of the convection cells, and the growth tips are stabilized by transport of bulk solution by the convective motion.

In our experiment, the gray-scale image of copper cellular morphology is given in Figure 4.27. The bulk solution penetrated into the spaces in between branches. No such cellular concentration distribution around the tips of branches is found to support Garik et. al.'s argument. The channel growth of copper deposition in parallel cells shows the bulk solution also penetrates into the spaces between the branches. The measured concentration distribution in channel growth of copper is given in Figure 4.14 and 4.16. No sign of cellular concentration around deposit tips is observed in the gray-scale image of copper channel growth (Figure 4.11 and 4.12).

In channel growth of zinc deposition as shown in Figure 4.19 (a), cellular convection induced at the growth tips is evident. The shape of these convection cells resembles the concentration distributions of Fleury and coworkers' observation (Figure 2.5) [43]. The concentration drops from the bulk value to nearly zero in between branches within one hundred micrometers at 0.02M in horizontal and 0.04M in vertical cell, where channel

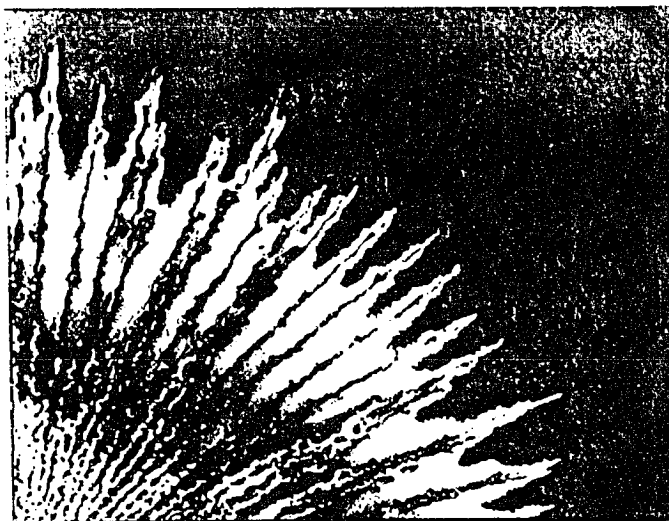


Figure 4.27: Gray-scale image of channel growth in deposition from 0.2M  $CuSO_4$  in a circular cell. anode diameter: 25 mm, cathode diameter: 1.0 mm, cell thickness: 250  $\mu m$  and image frame: 8638 $\mu m \times$  6858 $\mu m$ .

growth is produced (Figure 4.19 (b) 4.21 and 4.23 (b)). Contrary to copper channel growth, the bulk solution cannot penetrate into the spaces between branches in zinc channel growth. For zinc dendrites produced at 0.04M in horizontal cell (Figure 4.21) the concentration boundary layer is about 500 micrometers.

The significance of hydrodynamics in pattern selection is demonstrated by the shift from dendrites to channel growth when zinc deposition takes place in vertical cells instead of horizontal cells (Figure 4.20 and 4.18). Natural convection is suppressed in vertical configuration which causes the greater depletion of electrolyte at the interface. In binary solution, this condition can result in an appreciable space charge accumulation in the solution near the interface [77, 50]. In the horizontal configuration, while the interfacial concentration is still depleted to almost zero, natural convection prevents the development of a space charge accumulation by drawing fresh solution from the bulk to the interface. The arcs shown in vertical cell in Figure 4.20 (a) provides additional evidence that the cellular convection is produced by an electrokinetic effect. Natural convection in zinc deposition in horizontal cells is induced at higher concentrations, so that the channel growth is only observed at

low concentration. In the thinner cell used by Trigueros and coworkers [41], where natural convection is more strongly damped, they observed the shift to dendrites at a higher concentration than it occurs in our cells.

## 4.5 Electrokinetic Effects

The competition between the electric force and the gravity force due to the difference in electrolyte density between the interface and the bulk is evidenced in our experimental investigation of deposition from  $CuSO_4$  and  $ZnSO_4$  binary electrolyte solution in parallel cells. For deposition from  $ZnSO_4$ , morphological selection strongly depends on the configuration of the cells. For a given concentration of  $ZnSO_4$  in the range of 0.04M to 0.3M, an appropriate cell potential can always be found to form dendrites in horizontal cell while channel growth or other homogeneous growth in vertical cell as shown in Figure 4.5 and Figure 4.18.

We tried to find this dependence of morphology on cell configuration in electrodeposition from  $CuSO_4$ . However, no such dependence was observed. Since the transport parameters of ion  $Zn^{2+}$  and  $Cu^{2+}$  are nearly identical [73], we argue that it must be the difference of electrochemical kinetic parameters between  $CuSO_4$  and  $ZnSO_4$  that results in the difference of morphology dependence on cell configuration.

### 4.5.1 Theoretical Model

Theoretical and numerical analysis on the competition between the electric and gravity forces in the double layer are presented in this section. We assume each finger in electrochemical deposition to be in a steady state and to retain its parabolic shape in two-dimensional growth as shown in Figure 4.28.

The tip growth velocity  $V_0$  is constant for steady state crystal growth, the local velocity of the crystal growth normal to the crystal surface,  $V_n$ , is

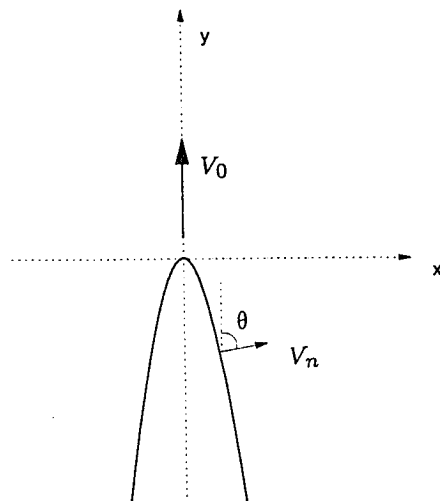


Figure 4.28: Schematic of a needle crystal with a parabolic shape.

$$V_n = V_0 \cdot \cos \theta \quad (4.19)$$

where  $\theta$  is the angle between the surface normal and the growth direction of the crystal.

Performing a material balance at any point on the crystal surface for steady state crystal growth gives

$$V_n(C_s - C_b) = \frac{i_n}{nF} \quad (4.20)$$

where  $C_s$  is the molar concentration of metal (density) of the aggregates and  $C_b$  the concentration of electrolyte in the bulk solution.  $i_n$  is the normal current density at the surface,  $n$  the charge number of the cation and  $F$  the Faraday constant.

A two dimensional parabolic crystal surface can be described by the following parabolic equation in cartesian coordinates

$$y = -a \cdot x^2 \quad (4.21)$$

where  $a$  is a shape constant which is measured from experimental images of electrodeposition.  $x$  and  $y$  are cartesian coordinates.

The total current,  $i_{total}$ , applied to a single crystal can be calculated from experimental data by dividing the overall current applied to a cell by the number of the crystals formed in the cell. The relation of the total current in each crystal and the local current density is given as

$$i_{total} = \int_s i_n ds \quad (4.22)$$

where the integral is taken over the entire crystal surface.

#### 4.5.2 Numerical Procedure and Results

By solving Equation 4.19, 4.20 and 4.22, the concentration of metal in the aggregates  $C_s$  can be calculated from experimental data as

$$C_s - C_b = \frac{i_{total}}{2nFV_0X} \quad (4.23)$$

where  $X$  is the width of a crystal at the base.

From our experiment, the density of metal in the aggregates,  $C_s$  is much less than that of solid metal since the aggregate is dispersed in solution. For example, the density of copper aggregates produced by deposition from 0.1M  $CuSO_4$  at 30 mA is  $9.257 \times 10^{-4}$  ( $mol/cm^3$ ), while the density of solid copper at room temperature is 0.1407 ( $mol/cm^3$ ).

By solving Equation 4.19 and 4.20, the local current density distribution on a crystal surface is obtained

$$i_n = nF(C_s - C_b) \cdot V_0 \cos \theta \quad (4.24)$$

For a parabolic equation given in Equation 4.21,  $\theta$  is given as



$$\cos \theta = \frac{1}{\sqrt{1 + 4a^2x^2}} \quad (4.25)$$

Thus, the local current density on a parabolic crystal surface is obtained

$$i_n = nF(C_s - C_b) \cdot \frac{V_0}{\sqrt{1 + 4a^2x^2}} \quad (4.26)$$

Let us assume that the local current density in the double layer very close to the crystal surface is the same as the local current density at the crystal surface. We further assume that the electric potential inside the crystal is identically uniform. The surface overpotential is defined as [69]

$$\eta_s = \Phi_s - \Phi \quad (4.27)$$

where  $\Phi_s$  is the electric potential of the crystal and  $\Phi$  is the electric potential in the solution adjacent to the surface of the crystal.

The current density depends on the driving force and thus is related to the surface overpotential and the composition of the solution at the interface, as well as the temperature. The Butler-Volmer equation is frequently used to describe this relation [69]

$$i_n = i_o \left[ \exp \left( \frac{\alpha_a F}{RT} \eta_s \right) - \exp \left( - \frac{\alpha_c F}{RT} \eta_s \right) \right] \quad (4.28)$$

This expression relates the surface overpotential  $\eta_s$  to the normal current density  $i_n$ ; the exchange current density  $i_o$  and the transfer coefficients  $\alpha_a$  and  $\alpha_c$ , which can be calculated from experimental data.

Equation 4.26, Equation 4.27 and Equation 4.28 are defined on the crystal surface only. By differentiating these equation in the tangential direction we obtain the potential gradient along the crystal surface,  $\vec{\nabla}_s \Phi$ .

The electrical force acting on the double layer in the tangential direction along the

crystal surface in unit volume of solution,  $F_v$ , is proportional to the charge density  $\rho_e$  and potential differential  $\vec{\nabla}_s \Phi$

$$F_v = \rho_e \cdot \vec{\nabla}_s \Phi \quad (4.29)$$

Though the charge density  $\rho_e$  is not estimated in this model, numerical simulation of  $\vec{\nabla}_s \Phi$  gives a qualitative explanation of the electrokinetic effects on pattern selection during electrodeposition.

As shown in Figure 4.29,  $\vec{\nabla}_s \Phi$  at the tip of a copper crystal is much greater than that of a zinc crystal. Thus, the electric force acting on an ion in the double layer in copper crystal growth is expected to be much greater than that in zinc crystal growth.

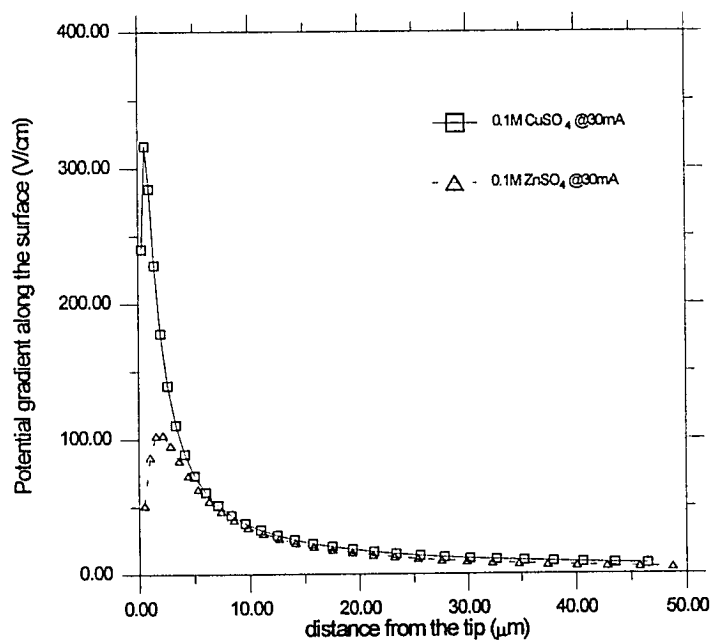


Figure 4.29: Comparison of the electric potential differential acting on a copper and zinc crystal surface in the tangential direction.

Based on these numerical results, we hypothesized that the electrical force acting at the

double layer near the tip of a crystal for deposition from  $CuSO_4$  is much greater than the gravity force. In both the vertical and horizontal configurations, the combined force drives the solution along the surface of the aggregates away from the tips. Since the flow pattern of the solution at the double layer near the tip is independent of the configuration, the growth pattern of aggregates is also independent of the cell configuration.

In the case of electrodeposition from  $ZnSO_4$  at very strong electric field as shown in Figure 4.29, the electrical force acting at the double layer near the tip of a crystal is comparable with or less than the gravity force. Thus the gravity force may have a significant effect on the flow pattern of electrolyte solution near the tips and play a crucial role in pattern selection as the configuration of a cell changes from horizontal to vertical.

## 4.6 Effects of Ohmic Heating

The effects of ohmic heating in an electrolysis cell during electrochemical deposition with binary electrolyte may be significant since the conductivity of the binary electrolyte solution without supporting electrolyte is low. The electrolyte concentration inside the concentration boundary layer near the aggregate interface is much lower than that of the bulk solution, and has an even lower conductivity. Therefore, the ohmic heating is greatest at the interface.

### 4.6.1 Adiabatic Cells

To study the ohmic heating effects on ECD in a parallel two-dimensional cell, the following assumptions have been made:

1. steady-state aggregate growth;
2. convection of the electrolyte solution is neglected, and
3. adiabatic cell with no heat transfer to the glass plates.

With these assumptions, as shown in Figure 4.30, the energy balance in a control volume is

$$\frac{i^2}{\kappa \cdot S} \cdot dt = \rho S dx \cdot C_p dT \quad (4.30)$$

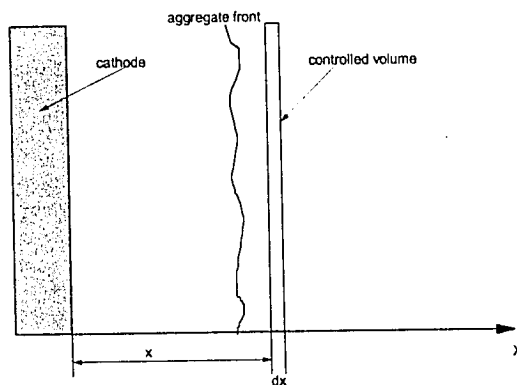


Figure 4.30: Schematic of a parallel cell to show the ohmic heating model

where the left hand side is the ohmic heat generated in the control volume, and the right hand side is the heat required to increase the temperature of  $dT$  for the solution in the control volume.  $\kappa$  is the local conductivity,  $S$  the cell cross area normal to the direction of current,  $\rho$  the density of the solution,  $C_p$  the specific heat,  $T$  the temperature, and  $t$  the time in seconds.

The ohmic heating process at any point in the cell during ECD can be divided into three regions:

1. The local conductivity is the same as that of the bulk before the boundary layer progresses to that point. Integrating Equation 4.30, the temperature increase is obtained as follows

$$\Delta T_1 = \frac{i^2 \cdot t}{\rho S^2 C_p \kappa_b} \quad (4.31)$$

2. When the point of interest is inside the concentration boundary layer, and before the aggregates reach the point, the temperature increase is the sum of the following

$$\Delta T_1 = \frac{i^2 \cdot t_0}{\rho S^2 C_p \kappa_b} \quad (4.32)$$

$$\Delta T_2 = \frac{i^2}{\rho S^2 C_p} \int_{t_0}^t \frac{dt}{\kappa(t)} \quad (4.33)$$

where  $t_0$  is the time required for the concentration boundary layer progresses to the point.

3. After the aggregates reach the point, the conductivity of the aggregates is much greater than that of the solution and the ohmic heating is negligible afterward. The temperature retains the same value as the aggregates just reach that point for an adiabatic cell.

The interferometric results show that the concentration distribution in the boundary layer is linear, so the concentration inside the boundary layer can be expressed as

$$C = C_i + \frac{(C_b - C_i)}{\delta} x' \quad (4.34)$$

where  $C_i$  and  $C_b$  are the concentration at the interface and in the bulk, respectively.  $\delta$  is the thickness of the boundary layer and  $x'$  is the distance from the interface to the point of interest inside the boundary layer.

The conductivity data of  $CuSO_4$  and  $ZnSO_4$  in various concentration is available in Dobos's handbook [73] and can be correlated as power function of concentration

$$\kappa = AC^b \quad (4.35)$$

where  $A = 0.283838$  and  $b = 0.796331$  are obtained from data regression for the concentration range from 0.005M to 0.5M.

The maximum temperature increase for an adiabatic cell is obtained by solving Equation 4.31, 4.32, 4.33, 4.34 and 4.35. The solutions are the sum of  $\Delta T_1$  and  $\Delta T_2$  any point with the distance of  $x > \delta$  from the cathode

$$\Delta T_1 = \frac{i^2}{\rho S^2 C_p} \frac{x - \delta}{AC_b^b v} \quad (4.36)$$

$$\Delta T_2 = \frac{i^2}{\rho S^2 C_p} \frac{(C_b^{1-b} - C_i^{1-b})\delta}{A(C_b - C_i)(1 - b)v} \quad (4.37)$$

where  $v$  is the aggregate growth velocity.

The interfacial concentration and the thickness of the boundary layer are obtained by interferometry. The computed adiabatic temperature increase is given in Figure 4.31.

Ohmic heating seems significant in adiabatic cells. However, when we mounted thermocouples 0.5 cm from the cathode to measure the temperature increases in a cell with the same experimental conditions as those given in Figure 4.31, the maximum temperature increase measured was 10°C, while it is predicted to be 52°C in the adiabatic model.

#### 4.6.2 Discussion

The adiabatic assumption is questionable because the electrolyte solution is in contact with two glass plates. Thermal conduction through the glass plates can not be neglected. As shown in Figure 4.32, the thickness of the glass plates is much larger than that of the electrolyte solution in between, and the heat capacity of the glass plates is 26.4 times greater.

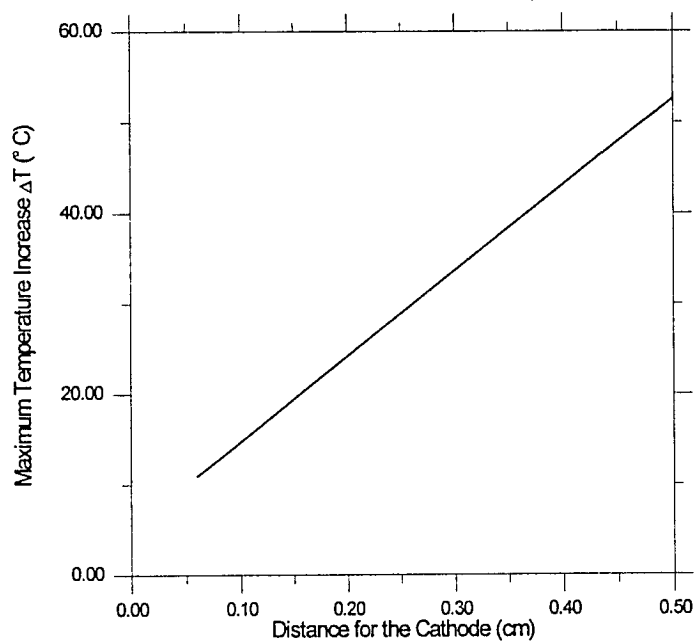


Figure 4.31: Theoretical results of ohmic heating in an adiabatic cell: ECD of 0.2M  $CuSO_4$ ; applied potential 15 V; cell spacing 250  $\mu m$ ; two electrodes 10 mm apart;  $C_i = 0.06M$ ;  $\delta = 0.06cm$   $i = 25mA$  and  $v = 18.3\mu m/s$ .

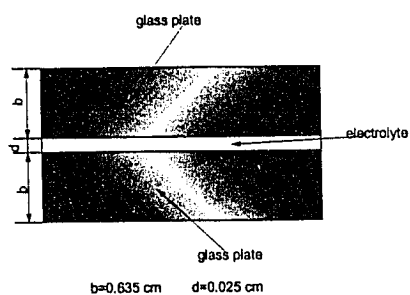


Figure 4.32: Schematic of glass plates and electrolyte solution in a parallel cell.

As in the case of deposition from  $CuSO_4$  as shown in Figure 4.31, the time required for the aggregates to grow to the distance of  $\delta$  and  $0.5\text{ cm}$  are 32.8 seconds and 273 seconds, respectively. The transient heat transfer theory gives a *penetration time* as follows: [74], (*penetration time* is defined as the time required for the temperature change at an interior point is 1% of the surface and initial temperature difference for the sudden change in boundary temperature in a semi-infinite slab.)

$$t = 0.0755 \frac{x^2}{\alpha} \quad (4.38)$$

where  $x$  is distance from a point of interest to the surface and  $\alpha$  is the thermal diffusivity of the glass ( $3.85 \times 10^{-3} \text{ m}^2/\text{s}$ ).

Since the thickness of glass plates is one quarter-inch in our experiment, the penetration time is only 7.9 seconds. In addition, the heat capacity of the glass plates is 26.4 times greater than that of the electrolyte solution in between. The assumption of adiabatic cells is, therefore, not justified.

The numerical simulation of the ohmic heating process in a cell is a two-dimensional unsteady state heat transfer problem. Ohmic heating is a unique phenomenon in electrochemical deposition which does not exist in any other pattern formation systems. Most theoretical models for aggregate growth in ECD are developed from the models for solidification and the ohmic heating effects have not been taken into account. This could be one of the reason for the discrepancy between the theoretical models and experimental measurement.

#### 4.6.3 Effect of Ohmic Heating on Concentration Measurements

In our interferometric measurement of the concentration boundary in an electrolysis cell, a uniform temperature is assumed. Since the effect of temperature on refractive index cannot be separated from that of solute content, it is important to know what temperature



variations can be tolerated in the measurement of concentration fields.

The temperature coefficient of the refractive index decreases linearly with increasing temperature [75]. The change in refractive index per  $^{\circ}C$  is  $1.88 \times 10^{-4}$  for a 1.0M  $CuSO_4$  solution at 18  $^{\circ}C$ . In our electrochemical deposition experiment as shown in Figure 4.31, the maximum temperature difference between the interface and bulk just outside the concentration boundary is 5  $^{\circ}C$  with the adiabatic assumption. The corresponding maximum measurement error in concentration due to temperature variation is in the order of 15%.

The real temperature variations should be much less than that estimated by the adiabatic assumption model and the concentration measurement error due to temperature variation in our interferometric studies should be acceptable.

## 4.7 Comparison with Velocity Selection Theories

Some important theoretical results developed for solidification are translated to the case of electrochemical deposition in this section. The theoretical results will be compared with experimental values. At constant applied potential, a needle crystal shape is found to be consistent with diffusion or ohmically controlled growth, which will be discussed separately.

### 4.7.1 Diffusion Controlled Growth Crystal

As discussed in chapter 2, the equations describing the electrochemical deposition system can be further simplified for binary electrolyte as in our experiment. If electroneutrality is assumed and convection is neglected, the general diffusion equation given in chapter 2 (Equation 2.8) reduces to a form analogous to the heat transfer or non-electrolytic mass transfer equation

$$\frac{\partial C}{\partial t} = D \nabla^2 C \quad (4.39)$$

For steady-state deposition, a material balance at the growth front gives

$$V_n(C_s - C_b) = \frac{i_n}{zF} = D \frac{\partial C}{\partial n} \quad (4.40)$$

where  $V_n$  is a normal growth velocity at any point of the aggregate front,  $D$  is the diffusivity,  $C_s$  is the concentration of metal in the deposits, and  $C_b$  is the bulk concentration.

The diffusion system in Equation 4.39 and 4.40 is more conveniently replaced by an equivalent Green function as in the case of solidification [2]. The concentration at the interface,  $C_i$  is given by an integral over the entire needle crystal surface

$$C_i(\mathbf{x}, t) = C_b + \int_{S'} dS' \int_{-\infty}^t dt' G(\mathbf{x} - \mathbf{x}', t - t') \frac{\partial C}{\partial n} \quad (4.41)$$

where  $dS'$  is an element of surface on the needle,  $\mathbf{x}$  is a position vector and  $n$  is the normal to the surface. Prime denotes the domain over which the integral is performed. The Green function  $G$  for the diffusion system is

$$G(\mathbf{x}, t) = \frac{\exp(-x^2/4Dt)}{4\pi Dt} \quad (4.42)$$

With the assumption of steady state growth, for a shape-preserving needle crystal, the normal local velocity is

$$V_n = V_o \cos \theta \quad (4.43)$$

where  $V_o$  is the growth velocity at the needle tip and  $\theta$  is the angle between the surface normal and the growth direction of the crystal.

If the growth rate is small and the cell current density is much smaller than the exchange current density  $i_o$ , the interface will be close to equilibrium. The activation can be neglected and the Butler-Volmer Equation 4.28 is simply replaced by the condition

$$\eta = 0 \quad (4.44)$$

If capillary is neglected, the concentration and potential at the crystal surface will be uniform. We use the Nernst equation [69] for the interfacial concentration

$$C_i = C_b \exp\left(-\frac{nF}{RT}\phi_o\right) \quad (4.45)$$

With these simplifications, the electrochemical deposition problem is reduced to a form analogous to solidification in which the dimensionless undercooling,  $\Delta$ , is replaced by

$$\Delta = 1 - \exp\left(-\frac{nF}{RT}\phi_o\right) \quad (4.46)$$

We use the results obtained for solidification [2]. The product of velocity,  $V_o$ , and the tip radius,  $\rho$ , is constrained to satisfy the following relation

$$1 - \exp\left(-\frac{nF}{RT}\phi_o\right) = e^p \sqrt{\pi p} \cdot \operatorname{erfc}(\sqrt{p}) \quad (4.47)$$

where  $p$  is the Peclet number.

$$p = \frac{\rho V_o}{2D} \quad (4.48)$$

The results of equation 4.47 is shown in Figure 4.33. The tip radius,  $\rho$ , increases with increasing potential,  $\Phi_o$ . In contrast, the opposite is true in our experiments on zinc deposition. As shown in Figure 4.4, the higher the applied potential, the smaller is the tip radius,  $\rho$ . This apparently results from the over-simplification of this model that makes it inconsistent with the experiment for electrochemical deposition system. The boundary conditions are evidently critical to the selection problem.

As discussed in Chapter 2, Section 2.5, a more complicated boundary condition, such as one that includes surface tension, kinetic overpotential and anisotropy must be introduced into the theoretical model. With these "microscopic solvability" conditions, the solution to an integral Equation 4.41 is an eigenvalue problem for the velocity and only a discrete set

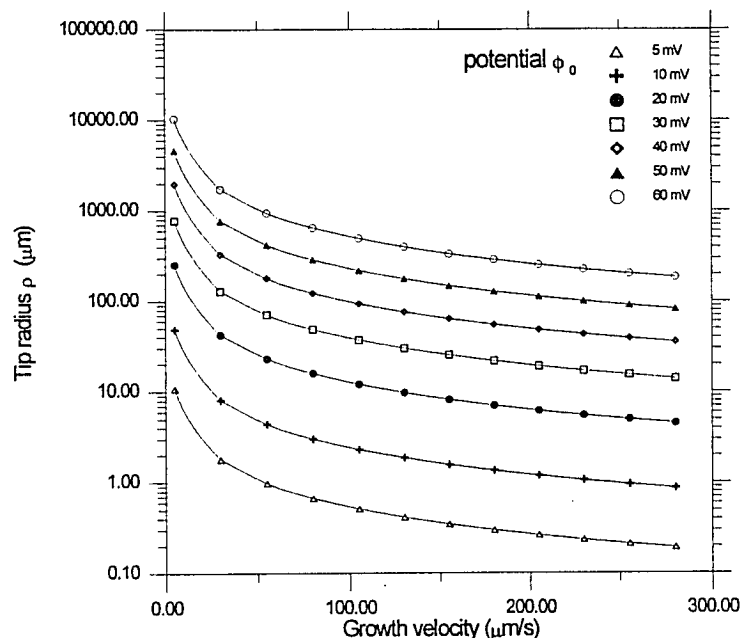


Figure 4.33: Theoretical relationship of crystal tip radius and growth velocity as the function of applied potential.

of velocities can meet this condition. Further theoretical investigation could be done and the theoretical results from models with more complex boundary conditions could be tested against experimental data in further research.

#### 4.7.2 Ohmic Controlled Growth Crystal

For ohmic controlled growth, we neglect the kinetic and concentration overpotential contribution to the overall potential in a cell. Only the primary distribution is taken into account here. With these assumptions, the metal surface was at constant potential,  $\Phi_o$ , and we have

$$i_n = \kappa \cdot \nabla \Phi \quad (4.49)$$

where  $\kappa$  is the conductivity of the electrolyte solution. The Laplace's equation can be used here

$$\nabla^2 \Phi = 0 \quad (4.50)$$

The potential at any point  $\mathbf{x}$  is given by the surface integral

$$\Phi(\mathbf{x}) = \Phi_o = \int \left( G \frac{\partial \Phi}{\partial n} + \Phi \frac{\partial G}{\partial n} \right) dS' \quad (4.51)$$

where  $G$  is the electrostatic Green function

$$G = \frac{1}{\mathbf{x} - \mathbf{x}'} \quad (4.52)$$

A parabolic tip is defined by

$$z = br^2 \quad (4.53)$$

where  $z$  is the coordinate in the growth direction,  $r$  the radial coordinate and  $b$  is the radius of curvature of the tip as shown in Figure 4.34.

Equation 4.51 is an eigenvalue problem for  $b$  for given potential  $\Phi_o$  and velocity  $V_o$ . We suppose that a needle emerges from a finite planar electrode or insulating surface, since the integral diverges if it is carried out to an infinite planar electrode.

Figure 4.35 gives computed values of tip radius  $\rho$  versus dendrite length in this study. The results shows that the relation between tip radius and velocity is strongly dependent on the length of the crystal for the case of a planar electrode but only weakly so for an insulating boundary. The computed tip radii are compared with Oren and Landau's <sup>[76]</sup> experimental data under the similar potential and growth velocity. The computed values are an order of magnitude larger than their measured values. This indicates that diffusion control is more significant than ohmic control in dendritic growth from well supported solution.

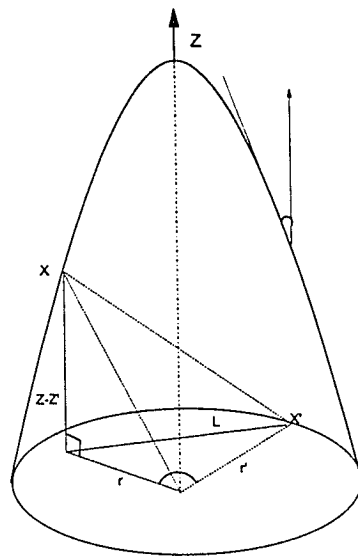


Figure 4.34: Schematic of a 3-dimensional needle crystal.

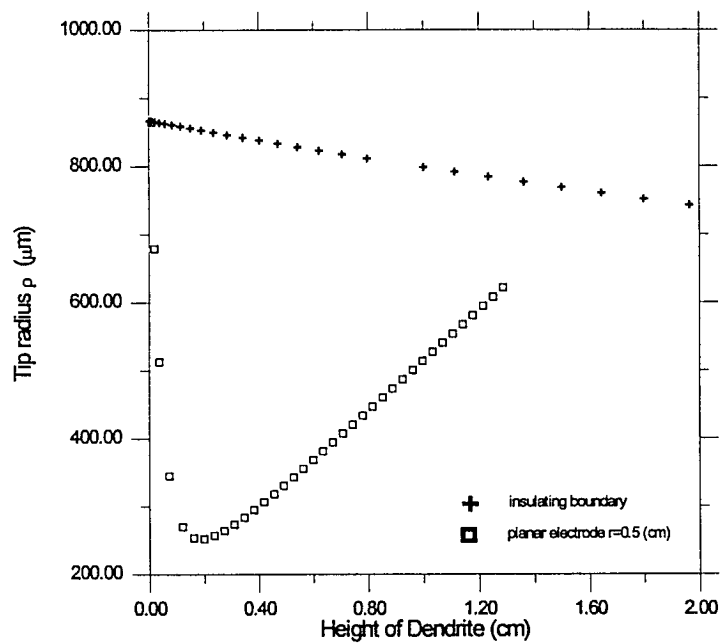


Figure 4.35: Computed tip radius versus dendrite height for insulating and conducting boundary. potential  $\Phi = 25\text{mV}$ , growth velocity  $v = 0.1\mu\text{m/s}$ .

# Chapter 5

## Conclusions and Recommendations

Convection induced by electrochemical deposition of zinc and copper from binary sulfate electrolyte in the two dimensional electrolysis cells used in pattern formation studies is observed in this study. The interferometric studies have shown that natural convection is evident during deposition from electrolyte of concentration 0.04M and higher in a horizontal cell of thickness 100  $\mu m$ .

Channel growth in zinc deposition from binary sulfate solution is different from that of copper deposition in appearance and concentration profile around the branches. For channel growth in zinc deposition, cellular convection, which probably is generated by electrokinetic streaming, is observed under conditions where natural convection is suppressed by deposition in a vertical configuration or by use of dilute zinc sulfate solution. In addition, zinc dendrites are produced in a horizontal cell under the same experimental conditions where natural convection is evident. In contrast to zinc deposition, channel growth from copper deposition can be produced in either the horizontal or vertical configuration.

A preliminary theoretical model is introduced to study the electrokinetic effects on channel growth of zinc and copper. The numerical results show that the electric force acting on the double layer close to the interface at the tip of copper aggregates is much larger than that of zinc aggregates because of the different kinetic parameters of zinc and copper. For this reason, we conclude that natural convection is of primary importance in

morphology selection for zinc deposition, but it is not for copper deposition under certain conditions.

Theoretical models developed in solidification are translated to the systems of electrochemical deposition. Preliminary numerical simulations show that the numerical results with the assumption of primary current distribution for diffusion and ohmic controlled growth does not predict the behavior of experimental dendritic growth.

A simplified theoretical model with the assumption of an adiabatic cell is proposed for the studies of ohmic heating effects in electrochemical deposition. The predicted temperature rises during deposition are much higher than the experimental values. Analysis from this model indicates that the errors for concentration measurement due to temperature rises are tolerable for electrochemical deposition in two dimensional cells at moderate applied potential.

Pattern formation in electrochemical systems is more complicated than in other systems. Caution must be taken when translating some theoretical works from other systems to electrochemical deposition. The following issues are recommended for further studies:

1. Experimental methods could be developed to measure the convection around the tips of aggregates formed from electrochemical deposition to test the cellular convection hypothesis and the electrokinetic model developed in this study.
2. The interferometric setup would be equipped with stronger lenses to increase the resolution of the images for concentration measurement so that the concentration profile at the tip of aggregates produced in vertical cells can be measured.
3. Numerical simulation of aggregate growth in electrochemical deposition with more complicated boundary conditions including anisotropic surface tension and kinetics, ie., "microscopic solvability" conditions, could be performed to test if the theoretical models developed from solidification are applicable to electrochemical systems.
4. Ohmic effects in two dimensional cells present an unsteady state two dimensional



heat transfer problem with moving boundaries. Numerical studies can be developed to accurately simulate the ohmic effects on morphology selection in electrochemical systems.

# Appendix A

## Interferometric Study of the Concentration Profile

### A.1 Introduction

Aggregate morphologies in electrodeposition depend on the concentration of the electrolyte solution, applied potential and the configuration of the cell as discussed in Chapter 2. In this chapter, we will investigate the principles of concentration measurement with various interferometric techniques and their application to the studies of electrochemical deposition.

Laser interferometric techniques are used for the real-time measurement of the electrolyte concentration profile in the electrolysis cells without causing any disturbance to the electrolyte concentration field. Reported interferometric techniques used for concentration measurement in the literature can be divided into three categories: conventional laser interferometry [53]–[61], holographic interferometry [64, 63, 62] and phase-shifted digital interferometry [35].

#### A.1.1 Conventional Laser Interferometry

Modified Fabry-Perot interferometers were used by O'Brein et al. for the measurement of the concentration distribution of  $CuSO_4$  [57],  $ZnSO_4$  [54, 55],  $(C_4H_9)_4NClO_4$  [56] in electrolysis cells and the concentration field of the electrolyte in the lead-acid battery [61].

McLarnon et al. used a Mach-Zehnder interferometer to measure the concentration

boundary layer of  $CuSO_4$  in an electrolysis cell with natural or forced convection [58, 59, 60]. Light deflection errors due to concentration gradients near the cathode in the interferometer were investigated [58].

A Jamin-type interferometer used for measurement of the concentration profile of  $CuSO_4$  is illustrated in Figure A.1 [53]. A laser beam from a helium-neon laser emitter is split into two beams by a Jamin plate  $J_1$  and travels through an electrolysis cell. One beam passes through the bulk electrolyte and the other beam through the region near the cathode where the concentration of the electrolyte is expected to change during electrolysis. The two beams are then recombined by a second Jamin plate  $J_2$ . Both beams have the same intensity and travel through the same distance.

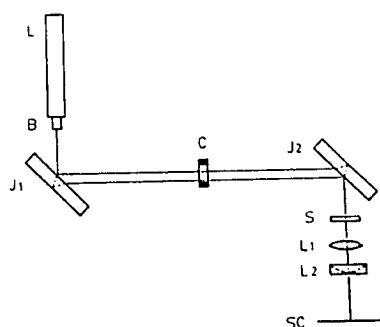


Figure A.1: Optical arrangement of Jamin-type interferometer (L: Ne-Ne laser emitter; B: beam expander;  $J_1$ ,  $J_2$ : Jamin plates; C: experimental cell; S: shutter;  $L_1$ ,  $L_2$ : optical lenses; Sc: screen). (after Nagatsutawa [53])

The glass windows of an electrolysis cell must be optically flat, homogeneous and all the mirrors and lenses for the optical apparatus must be clear of dust in order to obtain a clear image of interference for conventional laser interferometers.

Furthermore, the optical phase difference between the object and the reference waves must be great enough to allow more than one fringe to be formed. If the concentration change along the optical path is negligible, the equation for bright fringes can be simplified

to

$$n(x, y) - n_o = N(x, y) \cdot \frac{\lambda}{L}$$

where  $L$  is the thickness of the cell and  $N$  the fringe order.

### A.1.2 Holographic Interferometry

Holographic interferometric techniques have been used for the measurement of the concentration profile of the electrolyte solution of  $CuSO_4$  or  $AgNO_3$  in electrolysis cells [64, 63, 62].

The experimental arrangement is illustrated in Figure A.2 [64].

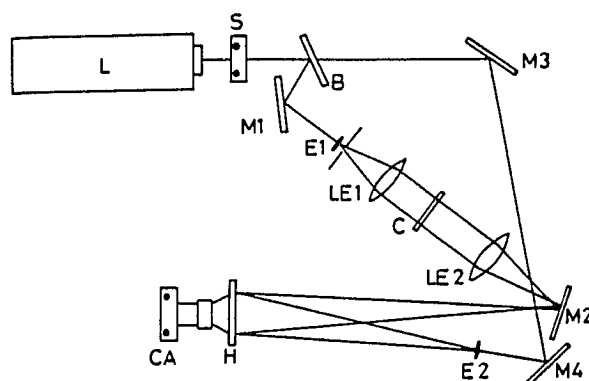


Figure A.2: Optical arrangement for holographic interferometry: L, laser; M1, M2, M3, M4, mirror; B, beam splitter; E1, E2, expander; LE1, LE2, lens; S, shutter; C, electrolysis cell; H, hologram; CA, camera. (after Fukunaka [64])

The laser beam from laser emitter  $L$  was split into two beams by a light splitter  $B$ . A reference beam was reflected on the mirrors  $M_1$  and  $M_4$  and was collimated by a lens  $E_2$ , and the beam intensity was adjusted by an attenuation polarizer  $A$ . Then the reference beam was transmitted to and focused on a photographic plate  $H$ . An object beam was reflected on the mirrors  $M_2$  and  $M_3$ , and was collimated by lens  $E_1$  and  $L_1$ . Then it passes through the region of a cell in the vicinity of the cathode and was focused on the same photographic plate by a lens  $L_2$  and a mirror  $M_3$ . After the electrolysis cell is set up and the light

beams are appropriately adjusted, a reference hologram is taken and developed. It is then reset at the same position. With the reference beam incident upon this hologram, the wave front of the beam which has passed through the electrolysis cell is reconstructed. This reconstructed wave is coincident with the beam which has passed through the electrolysis cell and a parallel interference fringe is obtained on a screen  $SC$ . After the beginning of electrolysis, the concentration of the electrolyte near the cathode and therefore the optical pathlength, change in that region. The fringe shift due to this optical pathlength change is

$$n(x, y) - n_o = N(x, y) \cdot \frac{\lambda}{L}$$

In a holographic interferometer only changes in pathlength between exposures are displayed on the screen. Pathlength errors due to the poor optical quality of a test window are present during both exposures and are therefore canceled. This is in contrast to conventional laser interferometers, where the pathlength variations in test section windows lead to errors in the fringe pattern which can be eliminated only by using optically flat, homogeneous windows.

### A.1.3 Digital Phase-Shifted Interferometry

Phase-shifted digital interferometry, developed by Watt and Vest for fluid mechanics applications [66, 67], is used in Barkey's [35] and this study to measure the concentration profile in electrochemical deposition. A phase-shifted digital Mach-Zehnder interferometer is schematically shown in Figure 3.3.

The minimum phase change due to concentration variations that a conventional laser interferometer or a holographic interferometer can detect is greater than  $2\pi$ . This is equivalent to that more than one fringe shift can be observed on the screen due to concentration variation. However, a digital phase-shifted interferometer can detect a very small optical phase change in the order of  $\pi/50$  [68]. Therefore, the former is only applicable to the mea-

surement of electrolyte concentration in a cell with the thickness of greater than 2 mm or in a cell with electrolyte concentration greater than 3 M, while the latter can be used for a cell of 100 μm thick with electrolyte concentration less than 0.1 M with acceptable accuracy. In the thicker cells, light deflection errors may not be neglected when conventional laser interferometers are used to measure the concentration of the electrolyte in a thick cell or a cell with concentrated electrolyte [58].

The pathlength errors due to the poor optical quality of a test window and to the difference of geometric alignment are present during both the reference state and the experimental exposures and the effects of these pathlength variations are canceled as in the case of holographic interferometry.

A digital phase-shifted interferometer is integrated in an electronic system in which the phase data is computed and recorded in a host computer, where it may be manipulated later. It takes less than a minute to obtain a reference phase map by computing the four interference maps with different phase shifts, while it takes at least half an hour to develop a reference hologram and to reset it back to its original position in holographic interferometer.

## A.2 Principles of Digital Phase-Shifted Interferometry

### A.2.1 Theory of Interference

Lasers emit narrow beams of nearly monochromatic light with almost perfectly plane wave fronts. The waves of laser light from the same source have the same frequency  $\omega$ , which can be represented in complex forms [65],

$$\Psi_1(r, t) = U_1 e^{i(k \cdot r_1 - \omega t)}$$

$$\Psi_2(r, t) = U_2 e^{i(k \cdot r_2 - \omega t)}$$

where  $\Psi$  represents the electric or magnetic field of the light,  $\omega$  is the frequency of the wave,  $k$  the wave number,  $U$  is the intensity of the light and  $r_1$  and  $r_2$  are the different distances through which the two laser beams travel.

The intensity at a point where the two waves interfere is given by [65]

$$I_T(x, y) = A(x, y)\{1 + M(x, y) \cos[\theta(x, y)]\} \quad (\text{A.1})$$

where  $A(x, y)$  is the amplitude function,  $M(x, y)$  is the modulation function, and  $\theta(x, y)$  the interferometric phase.

### A.2.2 Phase-Shifted Interferometry

The determination of the electrolyte concentration at a specific point of the cell requires the measurement of the optical phase before and after electrolysis at that point. The interferometric phase  $\theta(x, y)$  in Equation A.1 can be computed by introducing a number of known phase shifts and then sampling and storing the corresponding shifted interference patterns.

If the known phase shifts are given as  $\delta_i$ , the interference equation becomes

$$I_i(x, y) = A(x, y)\{1 + M(x, y) \cos[\theta(x, y) + \delta_i]\} \quad (\text{A.2})$$

For imaging equipment having the capacity to store four images in memory at any one time, four known phase shifts are chosen as

$$\delta_i = \frac{i \cdot \pi}{2} \quad i = 0, 1, 2, 3 \quad (\text{A.3})$$

Substituting Equation A.3 into Equation A.2, the phase term is given by

$$\theta(x, y) = \tan^{-1} \left( \frac{I_1 - I_3}{I_0 - I_2} \right) \quad (\text{A.4})$$

where  $I_i$  is the intensity value at a point for  $i$  phase shift.

A  $\pi/2$  phase shift is introduced by changing the pathlength of the reference beam by moving a mirror fastened to a piezoelectric translator by the amount of  $\lambda/4$ .

### A.2.3 Phase Change Computation

The CCD intensity information ( $I_i$ ) is relayed by an analog-to-digital converter and stored on a personal computer with Imaging Technology's FG-100 imaging board. The intensity value at each point [ $I_i(x, y)$ ] is represented by an integer of 0 to 255. The CCD camera digitizes an image into  $512 \times 512$  pixel elements, and 4 images with intensity information can be stored on the imaging board at any one time.

The phase  $\theta(x, y)$  given in Equation A.4 is the phase difference between the reference and object beams at any moment that the CCD camera is exposed. The undisturbed phase map of the reference state is recorded before the electrolysis cell is turned on, then a phase map can be recorded at any time during aggregate growth. The phase change map with the information of optical phase change due to concentration variation in the electrolysis cell can be obtained by subtracting the phase map of reference state from the phase map recorded during the aggregate growth.

The optical pathlength  $\Phi$  is defined as

$$\Phi = \int n dz$$

which is the path integral of the refracting index  $n$  along the ray path. The optical pathlength can be related to optical phase by,

$$\theta = \frac{2\pi}{\lambda} \Phi$$

For each experimental run, the phase term before electrolysis reaction takes place is



computed as a reference state. The optical phase is

$$\theta_{ref}(x, y) = \frac{2\pi}{\lambda} \cdot \int n_o dz + \Delta\theta_{geometry} \quad (A.5)$$

where  $n_o$  is the refractive index of the electrolyte solution with uniform concentration in the cell,  $\Delta\theta_{geometry}$  is the optical phase difference between the object and reference beams due to geometry difference.

When the power supply to the cell is turned on, the concentration of the electrolyte solution in the cell is changed and so is the refractive index. The optical phase difference of the system becomes

$$\theta(x, y) = \frac{2\pi}{\lambda} \cdot \int n(x, y) dz + \Delta\theta_{geometry} \quad (A.6)$$

The optical phase change due to concentration variations is obtained by subtracting Equation A.5 from Equation A.6

$$\Delta\theta(x, y) = \frac{2\pi}{\lambda} \cdot \int [n(x, y) - n_o] dz \quad (A.7)$$

The phase change at each pixel  $\Delta\theta(x, y)$  given in Equation A.7 is a discontinuous phase function modulo  $2\pi$ . The phase unwrapping procedure is to remove the  $2\pi$  modulus to retrieve the continuous phase function. A map of the fringe orders is created by the phase unwrapping procedure and is combined with the phase change map to yield a continuous total phase function, which is used for the evaluation of the electrolyte concentration profile in the cell. The transforming equation is given by

$$\Delta\theta_T(x, y) = \Delta\theta(x, y) + 2\pi \cdot O(x, y) \quad (A.8)$$

where  $\Delta\theta_T(x, y)$  is the total phase,  $O(x, y)$  is the fringe order.

To establish the fringe order  $O(x, y)$ , a procedure for distinguishing one order from

the next is needed, and whether the fringe order is increasing or decreasing needed to be identified. Leaving one order and entering another order is identified by a phase jump between two adjacent point. Once a discontinuity is detected, the point is assigned a higher or lower order fringe depending on the sign of the discontinuity in the fringe order  $O(x, y)$ . The fringe order of each point on the phase map is stored on a corresponding fringe order map and can be manipulated later.

#### A.2.4 Electrolyte Concentration Calculation

Once the total phase change is obtained, the local concentration of the electrolyte in the cell can be calculated with the correlation of refractive index  $n$  and concentration  $C$  of the electrolyte.

If the electrolyte is  $CuSO_4$  or  $ZnSO_4$ , the relation of the refractive index and the concentration is given as [58]

$$n = 1.3311 + 0.029C \quad (\text{A.9})$$

Assuming the concentration variation over the optical path of a cell is negligible, Equation A.7 can be simplified as

$$\Delta\theta(x, y) = \frac{2\pi}{\lambda} \cdot [n(x, y) - n_o]L \quad (\text{A.10})$$

where  $L$  is the thickness of a cell.

Obtaining the phase change  $\Delta\theta(x, y)$  from a phase change map from the phase unwrapping procedure, one can calculate the actual electrolyte concentration at the point in the cell by solving Equation A.9 and Equation A.10 simultaneously.

For a He-Ne laser with the wavelength  $\lambda = 0.633\mu m$  and the thickness of the cell of  $100\mu m$ , the maximum phase measurement error for this electronic Mach-Zehnder interferometer was  $\frac{\pi}{50}$  [68] and the error of  $CuSO_4$  concentration measurement for this technique

is not more than  $0.007 M$ . While for a conventional laser interferometer or a holographic interferometer, the resolution of concentration is not less than  $0.215 M$  since  $N$  must be greater than one for the fringe to be visible.

### A.2.5 Light Deflection Errors

For simplicity, assume that the refractive index of an electrolyte solution  $n$  varies in only one direction, which is perpendicular to the entering ray as in the cases of concentration measurement in electrochemical deposition. If the variation of  $n$  is linear, the approximate deflection is given for small concentration gradients, [65]

$$\frac{\Delta y}{\Delta z} = \frac{1}{2} \frac{dn}{dy} \cdot \Delta z \quad (\text{A.11})$$

where  $\Delta y$  is light deflection in the direction perpendicular to the entering ray,  $\frac{dn}{dy}$  is the gradient of refractive index and  $\Delta z$  is the thickness of the electrolysis cell.

For an experimental run of  $0.4M CuSO_4$  deposition at the potential of  $15V$  in a cell with the thickness of  $250 \mu m$ , the concentration boundary layer thickness is of the order of  $0.4 mm$ . The light deflection is

$$\frac{\Delta y}{\Delta z} = 0.0036$$

or the angle of light deflection is  $0.208$  degree, which is negligible. Moreover, proper placement of the imaging optics causes the beam deflection to be manifested only in a measured phase change.

## NOMENCLATURE

$A$  = surface area ( $m^2$ )

$b$  = radius of tip curvature ( $cm$ )

$C$  = concentration ( $mol/l$ )

$c_p$  = specific heat per unit volume ( $J/m^3K$ )

$d_0$  = capillary length ( $cm$ )

$D$  = diffusivity ( $cm^2/s$ )

$F$  = Faraday constant, 96,500 ( $C$ ) or force ( $N$ )

$G$  = Green function

$g$  = gravity acceleration ( $m/s^2$ )

$i$  = current density ( $A/m^2$ )

$i_o$  = exchange current density ( $A/m^2$ )

$I$  = light intensity ( $w/m^2$ )

$k$  = wave number

$L$  = characteristic dimension ( $m$ ) or latent heat per unit volume ( $J/m^3$ )

$M$  = atomic weight ( $g/mol$ )

$N$  = mass flux [ $kg/(m^2 \cdot s)$ ]

$n$  = number of electrons participating in an electrode reaction, unit normal or refractive index

$p$  = Peclet number or pressure ( $N/m^2$ )

$R$  = gas constant, 8.32 ( $J/mol \cdot K$ )

$r$  = radial coordinate

$S$  = surface area ( $m^2$ )

$T$  = temperature ( $K$ )

$t$  = time ( $s$ ) or ion transfer number

- $U$  = intensity of light ( $w/m^2$ )  
 $u$  = ion mobility  
 $V$  = growth velocity ( $m/s$ ) or electrode potential ( $V$ )  
 $v$  = growth velocity ( $m/s$ )  
 $x, y, z$  = cartesian coordinates  
 $z_i$  = number of charges in an ion.

### Greek Letters

- $\alpha$  = transfer coefficient  
 $\beta$  = kinetic factor  
 $\gamma$  = surface tension ( $N/m$ )  
 $\delta$  = thickness of boundary layer ( $cm$ )  
 $\epsilon$  = dielectric constant  
 $\eta$  = overpotential ( $V$ )  
 $\theta$  = angle between surface normal and growth direction ( $rad$ )  
 $\kappa$  = conductivity [ $(\Omega \cdot cm)^{-1}$ ]  
 $\lambda$  = wave length ( $\mu m$ )  
 $\mu$  = fluid dynamic viscosity ( $N \cdot s/m$ )  
 $\nu$  = kinematic viscosity ( $cm^2/s$ )  
 $\rho$  = density ( $kg/m^3$ )  
 $\Phi, \phi$  = potential ( $V$ ) or optical pathlength ( $\mu m$ )

**Subscripts**

$a$  = anodic

$b$  = bulk

$c$  = cathodic

$cn$  = concentration

$e$  = equilibrium

$i$  = interface

$l$  = limiting

$n$  = normal

$s$  = surface

**Superscripts**

$o$  = flat surface

# Bibliography

- [1] J. S. Langer, *Reviews of Modern Physics*, **52**, 1–28 (1980).
- [2] D. A. Kessler, J. Koplik and H. Levine, *Advances in Physics* **37**, 255–339 (1988).
- [3] E. A. Brener and V. I. Mel'nikov, *Advances in Physics* **40**, 53–97 (1991).
- [4] W. W. Mullins and R. F. Sekerka, *Journal of Applied Physics* **34**, 323–329 (1963)
- [5] W. W. Mullins and R. F. Sekerka, *Journal of Applied Physics* **35**, 444–451 (1964)
- [6] E. R. Rubinstein and M. E. Glicksman, *Journal of Crystal Growth*, **112**, 97–110 (1991).
- [7] E. R. Rubinstein and M. E. Glicksman, *Journal of Crystal Growth*, **112**, 84–96 (1991).
- [8] Y. Miyata, M. E. Glicksman and S. H. Tirmizi, *Journal of Crystal Growth*, **110**, 683–691 (1991).
- [9] N. B. Singh and M. E. Glicksman, *Journal of Crystal Growth*, **98**, 534–540 (1989).
- [10] M. E. Glicksman and N. B. Singh, *Journal of Crystal Growth*, **98**, 277–284 (1989).
- [11] M. A. Chopra, M. E. Glicksman and N. B. Singh, *Metallurgical Transactions A*, **19A**, 3087–3096 (1988).
- [12] M. E. Glicksman, E. Winsa, R. C. Hahn et. al., *Metallurgical Transactions A*, **19A**, 1945–1953 (1988).
- [13] J. Lipton, M. E. Glicksman and W. Kurz, *Metallurgical Transactions A*, **18A**, 341–345 (1987).

- [14] M. E. Glicksman and P. W. Voorhees, *Metallurgical Transactions A*, **15A**, 995–1001 (1984).
- [15] S.-C. Huang and M. E. Glicksman, *Acta Metallurgica*, **29A**, 717–734 (1981).
- [16] S.-C. Huang and M. E. Glicksman, *Acta Metallurgica*, **29A**, 701–715 (1981).
- [17] H. Lamb, “Hydrodynamics”, Cambridge University Press, London (1932).
- [18] G. Deutscher and Y. Lereah, *Physical Review Letters*, **60**, 1510 (1986).
- [19] E. Ben-Jacob, G. Deutscher, P. Garik, N. D. Goldenfeld and Y. Lereah, *Physical Review Letters*, **57**, 1903–1906 (1986).
- [20] E. Ben-Jacob, P. Garik, T. Mueller and D. Grier, *Physical Review*, **A38**, 1370–1380 (1988).
- [21] E. Ben-Jacob and P. Garik, *Nature*, **343**, 523–530 (1990).
- [22] J. S. Langer and H. Muller-Krumbhaar, *Acta Metallurgica*, **26**, 1681–1687, (1978)
- [23] J. S. Langer and H. Muller-Krumbhaar, *Acta Metallurgica*, **26**, 1689–1695, (1978)
- [24] H. Muller-Krumbhaar and J. S. Langer, *Acta Metallurgica*, **26**, 1697–1708, (1978)
- [25] M. N. Barber, A. Barbieri and J. S. Langer, *Physical Review*, **A36**, 3340 (1987).
- [26] D. A. Kessler, J. Koplik and H. Levine, *Physical Review*, **A30**, 3161 (1984).
- [27] D. A. Kessler, J. Koplik and H. Levine, *Ibid*, **31**, 1712 (1985).
- [28] E. Ben-Jacob, N. Goldenfeld, J. S. Langer and G. Schon, *Physical Review Letters*, **51**, 1930 (1983).
- [29] E. Ben-Jacob, N. Goldenfeld, B. G. Kotliar and J. S. Langer, *Physical Review Letters*, **53**, 2110–2113 (1984).



- [30] E. Ben-Jacob, N. Goldenfeld, J. S. Langer and G. Schon, *Physical Review*, **A29**, 330–340 (1984).
- [31] J. S. Langer, *Science*, **243**, 1150–1155, (1989)
- [32] Y. Saito, G. Goldbeck-Wood and H. Muller-Krumbhaar, *Physical Review Letters*, **58**, 1541–1544 (1987).
- [33] D. Barkey, *Journal of the Electrochemical Society*, **138**, 2912–2917 (1991).
- [34] D. Barkey, P. Garik, E. Ben-Jacob, B. Miller and B. Orr, *Journal of the Electrochemical Society*, **139**, 1044–1050 (1992).
- [35] D. Barkey, D. Watt, Z. Liu and R. Raber, *Journal of the Electrochemical Society*, **141**, 1206 (1994).
- [36] P. Garik, D. Barkey, E. Ben-Jacob, N. Broxholm, B. Miller, B. Orr and R. Zamir, *Physical Review Letters*, **62**, 2703–2706 (1989).
- [37] Y. Sawada, A. Dougherty and J. P. Gollub, *Physical Review Letters*, **56**, 1260–1263 (1986).
- [38] M. Matsushita, M. Sano, Y. Hayakawa, H. Honjo and Y. Sawada, *Physical Review Letters*, **53**, 286–289 (1984).
- [39] D. Grier, E. Ben-Jacob, R. Clarke and L. M. Sander, *Physical Review Letters*, **56**, 1264–1267 (1986).
- [40] F. Sagues, F. Mas, M. Vilarrasa and J. M. Costa, *Journal of Electroanal. Chem.*, **278**, 351–360 (1990).
- [41] P. P. Trigueros, J. Claret, F. Mas and F. Sagues, *Journal of Electroanal. Chem.*, **312**, 219 (1991).

- [42] F. Sagues, F. Mas, J. Claret, P. P. Trigueros and L. Lopez-Tomas, *Growth Patterns in Zinc Electrodeposition*, Proceedings of the NATO ARW on "Growth Patterns in Physical Sciences and Biology", Granada 7th. October, 1991.
- [43] V. Fleury, J. Kaufman and B. Hibbery, *Physical Review*, **E48**, 3831–3840 (1993).
- [44] V. Fleury, J.-N. Chazalviel and M. Rosso, *Physical Review*, **E48**, 1279–1295 (1993).
- [45] V. Fleury, J.-N. Chazalviel and M. Rosso, *Physical Review Letters*, **68**, 2492–2495 (1992).
- [46] V. Fleury, M. Rosso and J.-N. Chazalviel, *Physical Review*, **A43**, 6908–6916 (1991).
- [47] V. Fleury, *Journal of Material Research*, **6**, 1169–1174 (1991).
- [48] J.-N. Chazalviel, *Physical Review*, **A42**, 7355–7367 (1990).
- [49] V. Fleury, J.-N. Chazalviel, M. Rosso and B. Sapoval, *J. Electroanal. Chem.*, **290**, 249–255 (1990).
- [50] R. Bruinsma and S. Alexander, *J. Chem. Phys.*, **92**, 3074–3085 (1990).
- [51] J. O'M. Bockris and A. K. N. Reddy, "Modern Electrochemistry", Volume 2, Plenum Press, New York (1970).
- [52] G. A. Prentice and C. W. Tobias, *Journal of the Electrochemical Society*, **129**, 78–85 (1982).
- [53] I. Nagatsugawa, D. L. Piron and J. Bures, *The Canadian Journal of Chemical Engineering*, **69**, 1408–1412 (1991).
- [54] R. N. O'Brien, W. F. Yakymyshyn and J. Leja, *Journal of the Electrochemical Society*, **110**, 820–825 (1963).
- [55] R. N. O'Brien, J. Leja and E. A. Beer, *Journal of the Electrochemical Society*, **121**, 370–375 (1974).

- [56] R. N. O'Brien, and K. S. V. Santhanam, *Journal of the Electrochemical Society*, **130**, 1114–1117 (1983).
- [57] R. N. O'Brien, and P. M. Saville, *Journal of the Electrochemical Society*, **137**, 3797–3804 (1990).
- [58] F. R. McLarnon, R. H. Muller and C. W. Tobias, *Journal of the Electrochemical Society*, **122**, 59–64 (1975).
- [59] F. R. McLarnon, R. H. Muller and C. W. Tobias, *Electrochimica Acta*, **21**, 101–105 (1976).
- [60] F. R. McLarnon, R. H. Muller and C. W. Tobias, *Journal of the Electrochemical Society*, **129**, 2201–2206 (1982).
- [61] A. Eklund and R. N. O'Brien, *Journal of the Electrochemical Society*, **138**, 2212–2216 (1991).
- [62] Y. Awakura and Y. Kondo, *Journal of the Electrochemical Society*, **123**, 1184–1192 (1976).
- [63] Y. Fukunaka, T. Minegishi, N. Nishioka and Y. Kondo, *Journal of the Electrochemical Society*, **128**, 1274–1280 (1981).
- [64] Y. Fukunaka, T. Yamamoto and Y. Kondo, *Journal of the Electrochemical Society*, **136**, 3630–3633 (1990).
- [65] C. M. Vest, "Holographic Interferometry", John Wiley & Sons, New York (1979).
- [66] D. W. Watt and C. M. Vest, *Experiments in Fluids*, **5**, 401–406 (1987).
- [67] D. W. Watt and C. M. Vest, *Experiments in Fluids*, **8**, 301–311 (1990).
- [68] R. S. Raber, "Electro-Optic Interferometry with Noise Tolerant Phase Unwrapping", Master Thesis, *University of New Hampshire* (1991).

- [69] J. S. Newman, "Electrochemical Systems", Prentice-Hall, Englewood Cliffs, NJ (1973).
- [70] P. Garik, J. Hetrick, B. Orr, D. Barkey and E. Ben-Jacob, *Physical Review Letters*, **66**, 1606–1609 (1991).
- [71] A. J. Bard and L. R. Faulkner, "Electrochemical Methods", John Wiley & Sons, New York (1980).
- [72] D. G. Miller, J. A. Rard, L. B. Eppstein and R. A. Robinson, *Journal of Solution Chemistry*, **9**, 467–496 (1980).
- [73] D. Dobos, "Electrochemical Data", Elsevier Scientific Publishing Company, New York (1975).
- [74] F. White, "Heat and Mass Transfer", Addison-Wesley Publishing Company, Reading, Massachusetts (1988).
- [75] R. H. Muller, *Double Beam Interferometry for Electrochemical Studies*, in "Advances in Electrochemistry and electrochemical Engineering", P. Delahay and C. W. Tobias edited, Volume 9, John Wiley & Sons, New York (1973).
- [76] Y. Oren and U. Landau, *Electrochimica Acta* **27** 739–748 (1982).
- [77] V. G. Levich, "Physicochemical Hydrodynamics", Prentice Hall, Englewood Cliffs, NJ (1962).